Implosion dynamics measurements at the National Ignition Facility

D. G. Hicks, N. B. Meezan, E. L. Dewald, A. J. Mackinnon, R. E. Olson et al.

Citation: Phys. Plasmas **19**, 122702 (2012); doi: 10.1063/1.4769268
View online: http://dx.doi.org/10.1063/1.4769268
View Table of Contents: http://pop.aip.org/resource/1/PHPAEN/v19/i12
Published by the American Institute of Physics.

Implosion dynamics measurements at the National Ignition Facility

D. G. Hicks,[1,a)] N. B. Meezan,[1] E. L. Dewald,[1] A. J. Mackinnon,[1] R. E. Olson,[2] D. A. Callahan,[1] T. Döppner,[1] L. R. Benedetti,[1] D. K. Bradley,[1] P. M. Celliers,[1] D. S. Clark,[1] P. Di Nicola,[1] S. N. Dixit,[1] E. G. Dzenitis,[1] J. E. Eggert,[1] D. R. Farley,[1] J. A. Frenje,[3] S. M. Glenn,[1] S. H. Glenzer,[1] A. V. Hamza,[1] R. F. Heeter,[1] J. P. Holder,[1] N. Izumi,[1] D. H. Kalantar,[1] S. F. Khan,[1] J. L. Kline,[4] J. J. Kroll,[1] G. A. Kyrala,[4] T. Ma,[1] A. G. MacPhee,[1] J. M. McNaney,[1] J. D. Moody,[1] M. J. Moran,[1] B. R. Nathan,[1] A. Nikroo,[5] Y. P. Opachich,[1] R. D. Petrasso,[3] R. R. Prasad,[1] J. E. Ralph,[1] H. F. Robey,[1] H. G. Rinderknecht,[3] J. R. Rygg,[1] J. D. Salmonson,[1] M. B. Schneider,[1] N. Simanovskaia,[1] B. K. Spears,[1] R. Tommasini,[1] K. Widmann,[1] A. B. Zylstra,[3] G. W. Collins,[1] O. L. Landen,[1] J. D. Kilkenny,[1] W. W. Hsing,[1] B. J. MacGowan,[1] L. J. Atherton,[1] and M. J. Edwards[1]
[1]*Lawrence Livermore National Laboratory, Livermore, California 94550, USA*
[2]*Sandia National Laboratory, Albuquerque, New Mexico 87185, USA*
[3]*Massachusetts Institute of Technology, Cambridge, Massachusetts 02139, USA*
[4]*Los Alamos National Laboratory, Los Alamos, New Mexico 87545, USA*
[5]*General Atomics, San Diego, California 92121, USA*

(Received 13 October 2012; accepted 13 November 2012; published online 7 December 2012)

Measurements have been made of the in-flight dynamics of imploding capsules indirectly driven by laser energies of 1–1.7 MJ at the National Ignition Facility [Miller *et al.*, Nucl. Fusion **44**, 228 (2004)]. These experiments were part of the National Ignition Campaign [Landen *et al.*, Phys. Plasmas **18**, 051002 (2011)] to iteratively optimize the inputs required to achieve thermonuclear ignition in the laboratory. Using gated or streaked hard x-ray radiography, a suite of ablator performance parameters, including the time-resolved radius, velocity, mass, and thickness, have been determined throughout the acceleration history of surrogate gas-filled implosions. These measurements have been used to establish a dynamically consistent model of the ablative drive history and shell compressibility throughout the implosion trajectory. First results showed that the peak velocity of the original 1.3-MJ Ge-doped polymer (CH) point design using Au hohlraums reached only 75% of the required ignition velocity. Several capsule, hohlraum, and laser pulse changes were then implemented to improve this and other aspects of implosion performance and a dedicated effort was undertaken to test the sensitivity of the ablative drive to the rise time and length of the main laser pulse. Changing to Si rather than Ge-doped inner ablator layers and increasing the pulse length together raised peak velocity to 93% ± 5% of the ignition goal using a 1.5 MJ, 420 TW pulse. Further lengthening the pulse so that the laser remained on until the capsule reached 30% (rather than 60%–70%) of its initial radius, reduced the shell thickness and improved the final fuel ρR on companion shots with a cryogenic hydrogen fuel layer. Improved drive efficiency was observed using U rather than Au hohlraums, which was expected, and by slowing the rise time of laser pulse, which was not. The effect of changing the Si-dopant concentration and distribution, as well as the effect of using a larger initial shell thickness were also examined, both of which indicated that instabilities seeded at the ablation front are a significant source of hydrodynamic mix into the central hot spot. Additionally, a direct test of the surrogacy of cryogenic fuel layered versus gas-filled targets was performed. Together all these measurements have established the fundamental ablative-rocket relationship describing the dependence of implosion velocity on fractional ablator mass remaining. This curve shows a lower-than-expected ablator mass at a given velocity, making the capsule more susceptible to feedthrough of instabilities from the ablation front into the fuel and hot spot. This combination of low velocity and low ablator mass indicates that reaching ignition on the NIF will require >20 μm (~10%) thicker targets and laser powers at or beyond facility limits. © *2012 American Institute of Physics*. [http://dx.doi.org/10.1063/1.4769268]

I. INTRODUCTION

A. Ignition requirements and optimization

In the indirect-drive approach to inertial confinement fusion (ICF),[1–3] laser energy, converted to thermal x rays inside a high-Z cavity (hohlraum), ablatively drives the implosion of a spherical capsule containing a deuterium-tritium (DT) fuel layer. The resulting kinetic energy imparted to the fuel is converted at stagnation to a central hot spot inertially confined by colder, denser fuel.

The essential physics requirements for ignition can be intuitively grasped by considering the energy balance of the

a)hicks13@llnl.gov.

hot spot. When approaching the ignition threshold, the heat gained due to compression should exceed the heat lost through conduction and radiation. Delivering compressive work to the hot spot fast enough to overcome losses requires a high fuel velocity. Minimizing conduction and radiation loss demands that the hot spot be spherically symmetric and nearly free of cooler or higher-Z material driven into the core region by hydrodynamic instabilities. Inertially sustaining this net heating long enough to ignite a significant fuel fraction requires that the incoming fuel layer have a low enough adiabat that a high areal density is generated around the hot spot upon final convergence.

These requirements on the velocity and adiabat of the incoming fuel layer and the shape and mix fraction of the final hot spot can be combined into a single figure-of-merit such as the energy margin[4] or ignition threshold factor (ITF)[5] given by the ratio of available kinetic energy to the minimum required for ignition. Since the kinetic energy scales as V_f^2, where V_f is the fuel velocity, and the minimum required for ignition[6,7] scales as $\sim V_f^{-6}$, energy margin (or ITF) scales as V_f^8. This illustrates the critical importance of high velocities in the ICF hot spot ignition scheme. A value of 370 μm/ns is calculated to be at the ignition threshold.

Ignition requirements typically compete with each other. A fundamental trade-off is that between velocity and mix. Rocket-like[3,8] ablative acceleration of an ICF capsule achieves higher capsule velocities by removing ablator mass; however, too little remaining mass raises the risk of feed-through of ablation front instabilities into the fuel and hot spot.[9,10] This competition between velocity and mix ultimately sets the total laser energy required to achieve ignition since larger masses are more stable but require more energy to reach ignition velocity. Similarly, the velocity and adiabat requirements place competing demands on the laser pulse shape: High velocities are achieved with a high peak power delivered early in the pulse when the shell surface area is largest; low fuel adiabats are preserved by a slow increase in laser power to minimize shock entropy and can be compromised by pre-heat driven by high laser powers. The resulting optimized pulse shape has a long low power foot to minimize the adiabat and rises quickly to a high peak power to maximize the velocity.[11]

The National Ignition Facility (NIF)[12] laser was designed to operate at up to 1.8 MJ. On this energy scale, known uncertainties in high energy density physics models prevent an *a priori* determination of the experimental input parameters from radiation-hydrodynamic simulations alone. Additionally, uncertainties exist in the velocity, adiabat, shape, and mix *requirements* themselves: exactly satisfying all these requirements was previously thought to give a 50% chance the capsule will ignite.[13]

The National Ignition Campaign (NIC) was thus designed as a multi-dimensional experimental optimization of several different laser and target parameters, iteratively adjusting them to achieve ignition.[13–15] Starting from an initial "point design," 14 laser and 3 target parameters were to be adjusted based on data returned from 4 different types of experimental platform:[15] Surrogate (gas-filled) capsules ("*symcaps*") are used for measurements of the shape of the core (i.e., the central hot spot) to infer drive symmetry;[16] shock timing measurements in liquid deuterium are used to infer the fuel adiabat;[17,18] convergent ablator measurements are used to infer ablator velocity and mass;[19] Yield and ρR measurements[20,21] on cryogenic layered targets are then used to assess integrated performance[22,23] and mix.[24,25] These data have been used to progressively iterate the laser and target parameters to push implosion performance towards simultaneously meeting the requirements on velocity, adiabat, symmetry, and mix.

B. Background

This paper focuses on results from convergent ablator measurements on NIF ignition-scale implosions. The convergent ablator, or "*ConA*," experiments were designed to address uncertainties in the ability to predict the ablation pressure and mass ablation rate of the converging capsule. These lead to uncertainties in the final velocity and remaining ablator mass that determine the velocity-mix trade-off.

For ignition-scale NIF implosions, the mass of plasma ablated from the capsule ($\sim$3 mg) is 20–40 times larger than has been generated at previous laser facilities such as OMEGA[26] or NOVA[27] at comparable radiation temperatures ($\sim$300 eV). X rays produced at the hohlraum wall and in the coronal plasma must be transported through this blow-off to reach the capsule ablation front. Radiation transport through the plasma, which may not be in thermal equilibrium, is strongly affected by opacities[28–30] and equations-of-state (EOS)[31,32] and represents a major computational challenge. For example, in going from tens to hundreds of eV across an ablation front, carbon transitions from a Li-like to H-like ionization state, strongly affecting both opacity and EOS. Uncertainties in previous mass ablation rate measurements on smaller hohlraums at lower radiation temperatures[33,34] are magnified significantly when extrapolated to NIF-scale plasmas due to the larger optical depths involved.

Early hohlraum energetics measurements on the NIF,[35–38] though apparently successful in demonstrating sufficient laser-to-x-ray conversion efficiencies and tunable symmetry in surrogate capsules, persistently showed that the time at which peak x-ray emission from the imploded core occurred (referred to as the x-ray bang time (XRBT)) was 200–300 ps later than predicted by radiation-hydrodynamic simulations. This hinted that coupling of energy to the capsule was overestimated in the simulations. Implementation of the shock timing measurements indicated that those early energetics experiments were compromised by a severely suppressed laser picket, soon found to be caused by the presence of a few microns of target chamber condensate on the hohlraum laser entrance holes (LEH).[17] Fixing this problem resulted in an even larger bang time discrepancy, although at the time, it was not immediately clear that a late bang time guaranteed a low peak velocity. Subsequent improvements in shock timing, raising the laser picket further, and delaying the main pulse,[18] increased this discrepancy even more. It was during these earliest shock timing measurements, after diagnosing the LEH condensate problem, which the *ConA* measurements described here were begun.

The convergent ablator tuning strategy, as originally conceived, required measurements of the peak velocity and minimum mass of the ablator only.[13,15,39] Deviations from the design goal would then be reduced by changing the peak laser power and initial ablator thickness in an iterative approach demanding relatively few shots. Implicit in this strategy was that velocities of the point design would be within several percent of the ignition requirement and that the tuning landscape would be nearly linear and thus monotonic. As described below, first data showed that peak velocities of the 1.3 MJ Ge-doped polymer (CH) point design were ~25% below ignition requirements. Such a significant deviation from expectation meant that it would be difficult to achieve the required velocities within the energy and power constraints of the current NIF laser. Substantive changes in capsule designs, hohlraum designs, and laser pulse shapes, some of which had been anticipated before and others which were conceived during the experiments, would be necessary.

With ongoing experiments, it also became apparent that the measurement of shell velocity and mass needed to expand from being simply an "end state" measurement of conditions at peak velocity (after the laser turned off) to being a detailed mapping of the drive history via the observed implosion dynamics. The shock timing campaign, which uses continuous velocity interferometry to interrogate the drive pressure history during the foot of the pulse, is silent beyond the rise of the main pulse due to optical blanking of the leading shock wave.[17,18] There was thus a blind spot in the knowledge of the history of the drive on the capsule throughout the main laser pulse. By tracking the shell trajectory, mass, and thickness during this period, it has now been possible to fill in this gap and constrain the drive pressure history throughout the entire implosion.

C. Outline

Section II describes the setup of the implosion experiment, emphasizing the particular details of the *ConA* radiographic platform. Section III gives an overview and some new details about how analysis of the radiograph is performed and what experimental observables are extracted. Section IV provides a brief description of the simulations to which these measurements are compared. Section V goes through the suite of observables obtained on each group of shots, highlighting the main points. In Sec. VI, all these results and their implications are discussed, with conclusions given in Sec. VII. Readers interested in a summary assessment of these experiments, without extensive experimental details, can skip directly to Secs. VI and VII.

The convergent ablator experiments were performed within the broader context of the NIC, and thus incorporated influences and design changes motivated by other experimental platforms. The sequence of shots described in this paper reflects this evolution. Though it is not the purpose of this paper to explain the data from other platforms, brief mention will be given of the results or conjectures that motivated design changes to the *ConA* experiments described here.

The nature of an on-going experimental campaign is that new data often sheds a different light on past experiments. This paper presents plausible current interpretations of the results obtained thus far. There remain open questions whose resolution will await further experiments.

II. EXPERIMENTAL SETUP

The experimental setup for the various shots evolved over the course of the different campaigns. In this section, an overall summary is given of each experimental component: the laser, backlighter, hohlraum, capsule, and diagnostics, listing the different configurations. The motivation for each change will be described briefly, pointing out those design changes that were anticipated in the original tuning plan[13] and those that were not.

A. Laser conditions

The NIF[12] laser was designed to deliver up to 1.8 MJ at a wavelength of 0.35 μm. Its 192 beams are grouped into 48 quads with 16 quads comprising the inner cone of beams (oriented at 23.5° and 30° to the hohlraum axis) and 32 quads comprising the outer cone of beams (oriented at 44.5° and 50°). To enable cross-beam transfer for symmetry tuning,[40] inner and outer cone wavelengths were separated by several Angstroms. Wavelength separation was enabled between the 23.5° and 30° beams, once this capability was implemented.[41] Over the course of the experiments, the exact wavelength separations were adjusted according to the results from core emission symmetry measurements. All beams used continuous phase plates, smoothing by spectral dispersion, and polarization smoothing.[42] In these shots, laser energies into the hohlraum varied between 1 to 1.7 MJ, delivered on 184 beams. The remaining 8 beams (2 quads) were used to drive a backlighter foil.

A major focus of many of these shots was to investigate changes in the implosion dynamics observed with the rise time and duration of the main pulse. Nominal rise times to a peak power of 420 TW were 2 ns. Shots were taken with both 1 ns and 3 ns rise times, with many of the later shots using the 3 ns rise. Note that when changing the peak power, the slope of the rise remained the same, thus changing the duration of the rise. Nevertheless, the different slopes were still referred to as 1, 2, and 3 ns rises. The duration of the laser pulse was lengthened for many shots after it was discovered that the capsule acceleration appeared to decrease more rapidly than expected after the laser turned off. Several shots at the end of the experimental series used this longer "low coast" drive. While tuning the 4th rise duration was part of the original tuning plan, lengthening the main pulse was not.

B. Backlighter beams

Two outer quads were used to drive the backlighter foil with 35–60 kJ of energy in a pulse with a 1 to 2.4 ns flattop with a peak power of up to 2.2 TW/beam or 16–18 TW combined power. Initial shots looked late in time only, using shorter, lower energy pulses while later shots used the longer, higher energy pulses to view more of the target trajectory. The backlighter pulse was designed with a low-power

pre-pulse, arriving ~4 ns before the main pulse, to preform a plasma and increase x-ray conversion efficiency.[43]

Beams were pointed towards the 5 μm thick Zn backlighter foil positioned at 6 or 12 mm away from capsule center, a distance set by the need to avoid beam interference with the light shields surrounding the target. Using the standard outer cone phase plates generates a spot that is approximately 1.2 mm wide (oriented in the hohlraum equatorial plane) and 1 mm high when projected onto the foil. For shots designed to look late in the implosion when the capsule radius was $\lesssim$500 μm, all 8 beams were overlapped at a single spot giving a peak laser intensity of $\sim 2 \times 10^{15}$ W/cm^2. For shots looking earlier in time, the quads were pointed 1.2–1.4 mm apart, illuminating a 2.4 mm wide field of view with half the intensity.

C. Hohlraum design

The hohlraum length, diameter, and LEH diameter, as well as the hohlraum material were changed over the course of these shots. Though the original tuning plan had required only the hohlraum length be adjusted,[13] results from both symmetry and velocity measurements indicated the need to improve the hohlraum design. In all experiments, the hohlraum was filled with pure ^{4}He at a density 0.96 mg/cm^3, set by the earlier hohlraum energetics campaign.[35]

Initial experiments were performed using the point design hohlraum[5] which had a 5.44 mm inner diameter, 10.01 mm inner length, and a 3.101 mm diameter LEH at cryogenic shot temperatures (~24 K). After extensive measurements of core symmetry[16] showed that drive at the hohlraum waist was being depleted by optical scatter from the inner cone beams (resulting in a tendency toward oblate implosions), a shorter, wider hohlraum was implemented having a 5.75 mm inner diameter, 9.425 mm inner length (see Fig. 1(a)). This increased drive at the capsule waist from the outer cone beams, reducing demands on cross-beam energy transfer to the inner cone beams. To investigate possible laser clipping at the laser entrance hole, a larger diameter LEH (3.373 mm) was tested.[44] Though no evidence of clipping was found, there was found to be a nearly 10% loss in peak velocity (described below). This resulted in a return to the original 3.101 mm diameter LEH on subsequent shots.

In this last design configuration, tests were performed using both gold and uranium hohlraums. Gold hohlraum wall thicknesses were 30 μm. Uranium hohlraums had an 8.8 μm thick layer of depleted uranium inside an 18 μm thick gold wall. At peak hohlraum temperatures approaching 300 eV, uranium has a higher opacity and lower specific heat than gold and thus provides an increased x-ray conversion efficiency,[44] leading to higher capsule velocities for a given laser energy. The inside of the uranium layer was lined with a 0.6 μm gold layer, which protects the uranium from oxidation and also replicates conditions in Au hohlraums during the foot of the pulse. The various hohlraum design changes are listed according to shot number in Table III.

D. Capsule design

Capsules with CH-based ablators were used throughout this study. This glow-discharge polymer is composed of

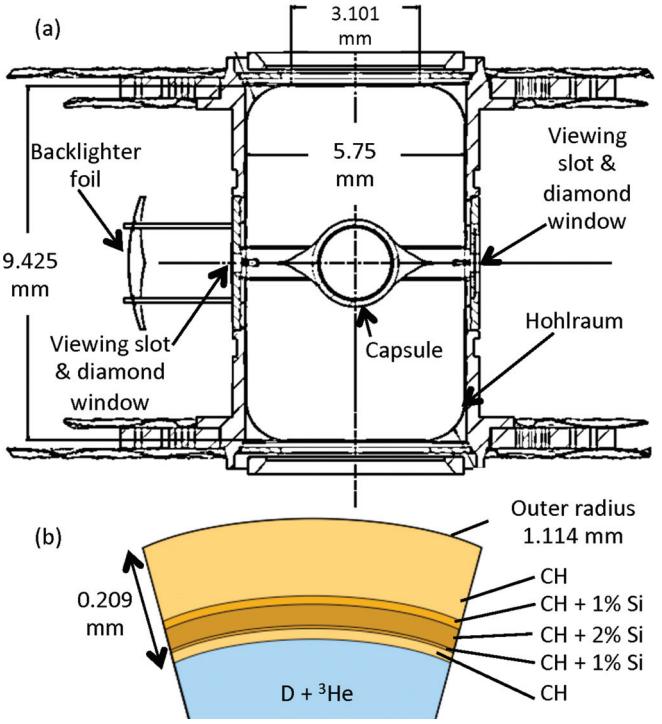

FIG. 1. (a) Target design showing the position of the zinc backlighter foil and the viewing slots through the hohlraum. Hohlraum dimensions are given for one type of design (see Table III). (b) Schematic of ablator showing dimensions for a graded Si-doped capsule (see Table I).

42.3% carbon, 57.2% hydrogen, and 0.5% oxygen by atomic fraction. After the first few shots, the ablator mid-Z dopant material was changed from germanium, set by the original point design,[5] to silicon in order to increase ablative drive pressure and thus peak capsule velocity. Most shots were performed with the resulting graded Si-doped design containing the stair-stepped 1%, 2%, 1% graded layered distribution[45] (see Fig. 1(b)). Towards the end of the experiments, a few shots used double the Si dopant concentration in each graded layer, and also a uniform Si dopant distribution. In addition, a single shot was performed with an ablator 20 μm thicker than the standard 209 μm thick design. The different types of target, the dopant concentrations, and layer densities are listed in Table I. Exact thicknesses and radii on a given shot, as well as the fill gas, are given in Table III. The original tuning plan anticipated that the ablator thickness and dopant concentration would need to be experimentally optimized;[13] having to adjust the dopant material and its distribution were not expected.

All but one of the shots utilized capsules filled with D-^{3}He gas, or *symcaps*. These gas-filled targets act as surrogates for targets containing solid DT or tritium-hydrogen-deuterium (THD)[46] fuel layers. Most gas-filled capsules contained 6.3 mg/cm^3 of 30:70 atomic deuterium to ^{3}He fraction set to 24 K at shot time. One shot was taken with a 50:50 D-^{3}He atomic fraction. This fill provides neutron yield at bang time and proton spectral[47] information at shock flash time (the arrival time at capsule center of a strong shock, just prior to final stagnation). Note that the gas fill pressure for *symcaps* (~3000 Torr) is around 60 times larger than the

TABLE I. Summary of capsule types used in these experiments, showing nominal dimensions, densities, and dopant concentrations at cryogenic shot temperatures (~24 K). Individual layer properties for the graded doped designs are listed in order from smallest radius to largest. In the case of the THD target, the mass given is for the ablator only. The actual (measured) outer radius and total thickness on a given shot vary slightly from these nominal values and are listed in Table III.

Capsule Type	Total CH Thickness (μm)	Outer Radius (μm)	CH Layer Thicknesses (μm)					CH layer Densities (g/cm^3)					CH layer dopant Atomic fraction (%)					Total Mass (mg)
Graded Ge-doped	203	1114	18	5	34	13	133	1.07	1.11	1.15	1.11	1.07	0.0	0.5	1.0	0.5	0.0	2.85
Graded Si-doped	209	1137	21	6	34	10	138	1.05	1.07	1.10	1.07	1.05	0.0	1.0	2.0	1.0	0.0	2.97
Graded Si-doped, THD	195	1130	6	6	34	10	139	1.05	1.07	1.10	1.07	1.05	0.0	1.0	2.0	1.0	0.0	2.77
Graded Si-doped, 2x	209	1137	21	6	34	10	138	1.05	1.08	1.12	1.08	1.05	0.0	2.0	4.0	2.0	0.0	2.98
Graded Si-doped, 2x thick	229	1157	20	6	35	10	158	1.05	1.08	1.12	1.08	1.05	0.0	2.0	4.0	2.0	0.0	3.33
Uniform Si-doped, 2%	205	1128	205					1.08					2.0					2.94

typical vapor pressure inside a layered DT target (50 Torr), leading to a lower convergence ratio (initial capsule radius divided by the minimum capsule radius) in *symcaps* compared to layered targets.

Gas-filled targets provide a practical platform for studying implosion dynamics without growing a cryogenic fuel layer. They also generate a neutron yield that is around a thousand times less than that from DT ignition targets, which along with the softer DD neutron spectrum, allows the CCD-based primary radiography diagnostics to be operated without concern for neutron damage. Most importantly, the primary goals of these shots are to characterize the implosion during the acceleration and peak velocity phase (i.e., at radii $\gtrsim$200 μm) where it is largely the total mass of the capsule that dominates the implosion dynamics. To be surrogates for the layered targets, gas-filled capsules thus have ablators containing an equivalent fuel mass payload of 14 μm of pure CH, located inside the shell. This mass is equivalent to that for ~69 μm of DT fuel. Note that surrogacy is not valid during the shock timing phase of the implosion since shock dynamics are different in capsules, which contain a fuel layer versus those which do not. In particular, shocks timed to coalesce deep in the fuel layer will be significantly mistimed if the ablator is thicker and has no fuel layer. Similarly, the different gas densities and release profiles inside the capsule result in different deceleration behavior at the end of the implosion. Thus, while the global dynamics of the surrogate implosion are expected to be similar, finer details will not be.

To test the validity of the surrogacy assumption, a single THD layered target was radiographed (Sec. V D). The fuel layer was composed of 74% T, 24% H, and 2% D by atomic fraction and held at 17.6 K.[23] Neutron yields were low enough to allow use of a standard CCD-based gated imager. On this shot, the fuel layer is transparent to the backlighter x rays; the experiment thus only measures the dynamics of the CH ablator. Of course such THD targets are themselves low-yield surrogates for DT ignition targets as has been described previously.[46] Radiographing DT targets is in principle possible in the future using radiation hardened imagers.

E. Radiographic imaging

Radiography was performed in the equatorial plane of the hohlraum using 8.95 keV He-α x rays from the laser-heated zinc backlighter foil. To provide equatorial line-of-sight through the capsule, two horizontal slots were cut around the hohlraum equator on opposite sides: the upstream slot (closest to the backlighter) provided access for the x rays while the downstream slot apodized the x ray illumination allowing only the equatorial plane of the capsule to be viewed (see Fig 1(a)). The original *ConA* targets, designed to look late during the implosion, had 1.2 mm wide slots (around the equator), allowing a view of capsule radii below ~500 μm. The more versatile *ConA-wide* design ("*ConAw*") had 2.4 mm wide slots and thus allowed viewing of capsules out to their starting radii of ~1 mm when backlighter beams were pointed accordingly. No obvious core asymmetry was caused by these slots.

Each hohlraum viewing slot was filled with a diamond sliver to prevent closure during the experiment. Each diamond sliver was 168 μm deep (i.e., in the hohlraum radial direction), resulting in 30% x-ray attenuation. The two slivers on a single target have different heights of 102 or 146 μm (in the hohlraum axial direction). The smaller sliver height was set by the maximum tolerable vertical blurring of the equatorial image slice. The larger sliver height was set by the beam divergence required to illuminate the vertical extent of the gated x-ray detector (GXD). Targets also had a 50 μm diameter tungsten wire on the downstream window, positioned to block some of the core self-emission, provide a background reference level for the analysis, and also act as a fiducial for checking the magnification within the x-ray images.

Early shots aligned the radiography axis with the diagnostic instrument manipulator (DIM)[48] in the 90–315 direction (i.e., in the equatorial plane, along the 315° azimuth). To better coordinate with the evolving needs of facility diagnostic transactions, later shots utilized the 90–78 diagnostic axis and DIM. Given that the target positioner axis is fixed (at 90–239 for the gas-filled targets, and 90–15 for the layered target), the change in viewing axis required targets with windows clocked at different positions. The primary result of this change was that the backlighter had to move from 6 mm away from capsule center to 12 mm for gas-filled targets since the backlighter foil was now closer to the 90–239 positioner axis where the target shield is wider (potentially interfering with the incoming backlighter beams). The THD-ConA target, since it was held on the 90–15 axis, could

TABLE II. Radiographic imaging setup for each shot: (a) The primary difference between the two target platforms used was in the length of the hohlraum slots cut around the equator for radiographic viewing. ConA (and THDConA) targets had 1.2 mm long slots, while ConAw targets had 2.4 mm long slots. (b) Experimental data recorded were either gated (GXD) or streaked (DISC); the numbers refer to the specific camera used. (c) Experiments were begun on DIM(90-315) and, to reduce facility transactions, switched to DIM(90-78). (d) Total magnification of the target at the image plane was measured on each shot using parallax of image features. The DISC internal magnification of 1.24 is included. (e) The imaging slit width in the snout was adjusted according to expected resolution requirements. (f) The field of view was 1.2 mm for measurements at late time only, and 2.4 mm for other measurements as fixed by the target platform and the backlighter pointing separation. (g) The distance of the slit to the target determined from the magnification.(h) Backlighter quads were set to be outer cone quads most opposite the DIM being used. (i) The distance of the backlighter foil from capsule center was set by the need for the beams to clear light shields. (j) Separation of the backlighter quad pointing positions was set by the required field of view. (k) Backlighter energies were higher for shots requiring viewing over a longer time window. (l) Backlighter peak powers were generally set near facility limits at the time of the shot.

	Apparatus			Imaging				Backlighter				
Shot #	(a) Target Platform	(b) Diagnostic	(c) DIM Azimuth (°)	(d) Mag	(e) Slit Width (μm)	(f) FoV (mm)	(g) Slit Dist (cm)	(h) Quads	(i) Distance (mm)	(j) Sep (mm)	(k) Energy (kJ)	(l) Pwr (TW)
N101218	ConA	GXD1	315	8.83	25	1.2	13.6	46 T/46B	6	0.0	37	16
N101220	ConA	GXD1	315	8.61	25	1.2	13.9	46T/46B	6	0.0	36	16
N110625	ConA	GXD1	315	8.71	25	1.2	13.8	46T/46B	6	0.0	36	16
N110627	ConA	GXD1	315	8.73	23	1.2	13.7	46T/46B	6	0.0	36	16
N110630	ConA	GXD1	315	8.76	26	1.2	13.7	46T/46B	6	0.0	37	16
N111007	ConAw	GXD3	315	8.81	30	2.4	13.6	46T/46B	6	1.2	54	18
N111009	ConA	GXD3	315	8.74	26	1.2	13.7	46T/46B	6	0.0	39	17
N111011	ConA	GXD3	315	8.79	28	1.2	13.6	46T/46B	6	0.0	39	17
N111218	ConAw	GXD3	315	8.69	9	2.4	13.8	46T/46B	6	1.2	58	18
N111219	ConAw	GXD3	315	8.78	30	2.4	13.7	46T/46B	6	1.2	57	17
N111220.1	ConAw	GXD3	315	9.06	27	2.4	13.3	46T/46B	6	1.2	57	17
N111220.2	ConAw	GXD3	315	8.69	11	2.4	13.8	46T/46B	6	1.4	57	18
N120119	ConAw	GXD3	315	8.78	10	2.4	13.7	46T/46B	6	1.2	58	18
N120121	ConAw	GXD3	315	8.76	10	2.4	13.7	46T/46B	6	1.2	56	17
N120122	ConAw	GXD3	315	8.74	28	1.2	13.7	46T/46B	6	0.0	57	18
N120123	ConA	GXD3	315	9.04	26	1.2	13.3	46T/46B	6	0.0	58	18
N120306	ConAw	GXD3	78	9.22	30	1.2	13.0	26B/31T	12	0.0	54	16
N120324	ConAw	DISC3	78	14.72	31	1.2	10.1	26B/31T	12	0.0	39	15
N120329	THDConA	GXD3	78	14.84	29	1.2	8.1	26B/31T	6	0.0	39	16
N120408	ConAw	DISC3	78	15.11	17	1.2	9.9	26B/31T	12	0.0	47	16
N120409	ConAw	DISC3	78	15.08	17	1.2	9.9	26B/31T	12	0.0	48	16
N120418	ConAw	DISC3	78	15.14	20	1.2	9.8	26B/31T	12	0.0	49	16
N120421	ConAw	DISC3	78	15.19	10	1.2	9.8	26B/31T	12	0.0	49	16

maintain the 6 mm backlighter standoff. These configuration changes, given shot-by-shot in Table II, did not cause any obvious systematic differences to data quality.

Most data were recorded on a microchannel plate-based GXD,[49,50] which gave a time resolution of ~105 ps for each image. Imaging was achieved using slits located at ~13.3 cm from target center and oriented 90° to the hohlraum slots, giving a magnification of 9× to the image plane. With *ConA* targets, 3 adjacent imaging slits were used, spaced horizontally 1.2 mm apart. Slits were ~25 μm wide, giving a spatial resolution ~10% worse than this. The GXD recorded a time sequence of discrete images on 4 separate strips spaced 300–350 ps apart, with 3 images per strip each spaced ~70 ps apart (for a total of 12 images per shot). With *ConAw* targets, the wider field of view (and the same magnification) required using only 1 imaging slit, giving a total of 4 images per shot. For some of the *ConAw* targets used to look early during the implosion when the shell was expected to be $\lesssim$25 μm, a 10 μm slit was used to improve spatial resolution. Imaging slits were machined in 200 μm thick Ta substrates to minimize the hard x-ray background.

The actual magnification for each shot was measured *in situ* using either the relative position of the wire in the 3 adjacent images on the ConA targets, or using the spacing of pinhole images of core emission obtained on an image plate positioned around the primary radiography imaging axis. This accounted for DIM insertion depth errors and gave residual uncertainties in magnification of ~1%. Measured magnifications, DIM offsets, and slit width for each shot are shown in Table II. The actual slit widths are used in the deconvolution of the data described below.

Later data were recorded on the DIM-based imaging streak camera (DISC),[51,52] giving a continuous record with ~70 ps time resolution (as set by the camera slit width and internal blurring). An ultraviolet temporal fiducial system[52] was used to check and calibrate sweep speeds on some shots. The smaller detector area resulted in lower counts per unit time than was obtained on the GXD but the continuous record in time allowed some of this loss to be regained at the expense of some time averaging. Data were taken primarily using a ~17 μm slit, although a 10 μm slit was used on one shot. Though providing a continuous record and more

TABLE III. Essential capsule, hohlraum, and laser parameters for each shot, along with some key neutron and x-ray core emission results. (a) Ablator thickness at shot temperature; (b) Outer radius of ablator at shot temperature; (c) Dopant type; All are graded doped except Si 2%, which is uniform doped. Si2x corresponds to 2× Si concentration in the doped layers; (d) Gas fill in atomic %; all used 30%D + 70%^{3}He apart from a single 50%D + 50%^{3}He shot and a layered THD shot. (e), (f), (g), (h): Hohlraum material and inner dimensions; Laser wavelength separation between (i) 30° beams and outer beams, and (j) 23° beams and 30° beams; (k), (l): Laser energy and peak power incident at the LEH (thus does not include backlighter beams); (m) Rise time of the main (4th) pulse, as specified for a 420 TW drive (lower peak powers have shorter rise times, such that the slope is preserved); (n), (o) Primary neutron yield and Doppler-inferred ion temperature. For D-^{3}He fills, this refers to the D-D yield; for the THD fill this corresponds to the DT yield; (p) X-ray bang time refers to the time of peak x-ray emission as measured by DIM-based framing cameras or by the south-pole bang time diagnostic (or both); (q), (r), (s): Legendre modes of the integrated x-ray core emission (at stagnation), as measured by DIM-based framing cameras.

	Capsule				Hohlraum				Laser @ LEH					Neutron		X-ray core			
Shot #	(a) Abl Thk μm	(b) Outer Radius μm	(c) Dopant	(d) Fill at%	(e) Mat'l	(f) LEH Diam mm	(g) Inner Length mm	(h) Inner Diam mm	(i) $\Delta\lambda_2$ Å	(j) $\Delta\lambda_{32}$ Å	(k) Energy MJ	(l) Peak Pwr TW	(m) 4th rise ns	(n) Primary Yield 10^{11}	(o) T_{ion} keV	(p) Bang Time ns	(q) m_0 μm	(r) P_0 μm	(s) P_2 μm
N101218	201.3	1127.9	Ge	30/70D^{3}He	Au	3.101	10.010	5.44	6.0	0.0	1.045	302	2	1.5	2.95	16.70	50	52	4
N101220	200.7	1123.7	Ge	30/70D^{3}He	Au	3.101	10.010	5.44	6.0	0.0	1.094	326	2	6.5	2.70	21.64	59	52	−13
N110625	203.4	1112.8	Ge	30/70D^{3}He	Au	3.101	10.010	5.44	8.0	0.0	1.332	430	2	2.2	2.26	22.40	43	62	5
N110627	209.8	1144.5	Si	30/70D^{3}He	Au	3.101	10.010	5.44	8.0	0.0	1.335	434	2	7.2	2.87	22.44	52	50	1
N110630	209.2	1139.8	Si	30/70D^{3}He	Au	3.101	10.010	5.44	8.0	0.0	1.416	433	2	3.9	2.50	22.43	57	60	−2
N111007	205.5	1130.7	Si	30/70D^{3}He	Au	3.101	9.425	5.75	7.5	1.0	1.291	428	2	2.9	2.41	22.42	40	56	13
N111009	206.4	1135.9	Si	30/70D^{3}He	Au	3.101	9.425	5.75	7.5	1.0	1.516	422	2	7.4	2.92	22.39	52	49	10
N111011	206.3	1138.2	Si	30/70D^{3}He	Au	3.101	9.425	5.75	7.5	1.0	1.270	419	2	4.7	2.52	22.51	52	60	8
N111218	206.3	1130.7	Si	30/70D^{3}He	Au	3.373	9.325	5.75	6.6	1.5	1.195	426	2	7.2	2.21	22.51			
N111219	209.3	1143.5	Si	30/70D^{3}He	Au	3.373	9.325	5.75	6.6	1.5	1.403	422	2	4.4	2.40	22.38	56		
N111220.1	208.4	1134.9	Si	30/70D^{3}He	Au	3.373	9.325	5.75	6.6	1.5	1.417	428	3	2.7	2.42	22.47	53	61	5
N111220.2	206.6	1132.7	Si	30/70D^{3}He	Au	3.373	9.325	5.75	6.6	1.5	1.406	430	1	3.8	2.51	22.20	62	67	4
N120119	208.5	1136.7	Si	30/70D^{3}He	Au	3.373	9.325	5.75	6.6	1.5	1.398	427	3	3.2	2.41	22.91		56	8
N120121	209.0	1139.9	Si	30/70D^{3}He	Au	3.373	9.325	5.75	6.6	1.5	1.377	420	1	3.8	2.34	22.53		64	−3
N120122	205.9	1125.3	Si	30/70D^{3}He	Au	3.373	9.325	5.75	6.6	1.5	1.388	426	3	3.6	2.39	22.89		55	−2
N120123	207.7	1129.2	Si	30/70D^{3}He	Au	3.373	9.325	5.75	6.6	1.5	1.383	423	1	4.1	2.44	22.57		63	3
N120306	208.2	1139.3	Si	30/70D^{3}He	U	3.101	9.425	5.75	7.3	1.2	1.530	340	3	5.0	2.50	23.00	38	51	15
N120324	208.7	1142.1	Si	30/70D^{3}He	U	3.101	9.425	5.75	7.3	1.2	1.498	334	3	5.0	2.45	22.90	38	37	6
N120329	192.6	1126.2	Si	74/24/2THD	Au	3.101	9.425	5.75	7.3	1.2	1.633	367	3	140.0	2.73	22.88	23	27	4
N120408	206.8	1143.7	Si2x	30/70D^{3}He	U	3.101	9.425	5.75	7.3	1.2	1.533	341	3	2.7	2.29	22.90	41	37	4
N120409	207.2	1146.3	Si2x	30/70D^{3}He	U	3.101	9.425	5.75	7.3	1.2	1.652	393	2	3.1	2.61	22.74	51	37	6
N120418	231.3	1168.8	Si2x	30/70D^{3}He	U	3.101	9.425	5.75	7.3	1.2	1.701	389	3	5.9	2.63	23.92	48	33	4
N120421	202.7	1128.1	Si2%	30/70D^{3}He	Au	3.101	9.425	5.75	7.3	1.2	1.632	367	3	0.9	1.50	22.58	60	38	4

aesthetically appealing images, and also better spatial and temporal resolution late in time, implementation of the streak camera did not change any of the conclusions obtained using the GXD. Note that, although the data appears continuous, any practical application has to bin the data over finite time intervals in order to achieve adequate signal-to-noise levels.

F. Other diagnostics

A range of secondary diagnostics were used to gather information on the x-ray, optical, and nuclear performance of each implosion. Though the emphasis of this paper is on the results from the x-ray radiography measurements, data from these secondary diagnostics will be selectively mentioned where relevant to the main themes of this paper.

An indirect measure of the kinetic energy coupled to the capsule is given by the XRBT. This was measured using gated x-ray imagers[49] located on the polar DIM and also, once commissioned, the south pole bang time (SPBT) time-of-flight diamond detector.[53,54] The shape of the core x-ray emission was measured using both gated imagers (for time-resolved data) but primarily using image plates (to give time-integrated shape). The image plate data were collected using a pinhole array in the equatorial and polar DIMs. Polar data were decomposed into Fourier components while equatorial data were decomposed into Legendre components.[55] A suite of neutron time-of-flight detectors[56] were used to measure the integrated neutron yield and Doppler-inferred average ion temperature of the core at nuclear bang time. In addition, compact proton spectrometers were used to measure the time-integrated downshifted spectrum of protons generated when a large shock reaches capsule center, a few hundred picoseconds prior to maximum compression.[47]

X-ray emission from the hohlraum was measured by the Dante broadband soft x-ray spectrometer[57,58] while the static x-ray imager (SXI)[59,60] was used to characterize the time-integrated behavior of the hohlraum wall and LEH. Hot electron levels were estimated using hard x-ray bremsstrahlung measurements (the filter-fluorescer experiment diagnostic, or FFLEX).[61] In addition, a full aperture backscatter system

(FABS) and the near backscatter imager (NBI) instrument separately measured the stimulated Brillouin and stimulated Raman scattered light from which the total backscattered power was determined.[62]

III. RADIOGRAPHIC OBSERVABLES AND ANALYSIS

A robust technique was developed previously[19] to extract information about the shell density distribution from time-resolved x-ray radiographs of the capsule. Observables from this technique and how they relate to ignition metrics, as well as the essential elements of the analysis, and recent improvements, are described.

A. Measurement observables and ignition requirements

The objective of this measurement is to extract radial moments of the density profile for the unablated (remaining) portion of the ablator. The radiographic analysis is able to extract low-order density moments accurately even though information about high-order features may be limited by instrument resolution.

For a given radial density profile, $\rho(r)$, the remaining ablator center-of-mass ($\langle R_m \rangle$), velocity ($\langle U_m \rangle$), areal density ($\langle \rho \mathrm{R} \rangle$), mass ($M$), and shell thickness ($2\sigma$) are defined as follows:

$$\langle R_m \rangle = \frac{\int r\rho(r) r^2 \, \mathrm{d}r}{\int \rho(r) r^2 \, \mathrm{d}r}, \tag{1}$$

$$\langle U_m \rangle = \frac{\mathrm{d}\langle R_m \rangle}{\mathrm{d}t}, \tag{2}$$

$$\langle \rho \mathrm{R} \rangle = \int \rho(r) \, \mathrm{d}r, \tag{3}$$

$$M = 4\pi \int r^2 \rho(r) \, \mathrm{d}r, \tag{4}$$

$$2\sigma = 2\frac{\int \rho(r)(r - \langle R_m \rangle)^2 \, \mathrm{d}r}{\int \rho(r) \, \mathrm{d}r}. \tag{5}$$

The radiographic absorption measurement measures only ablator quantities and does not directly record information about the gas fill or, in the case of the layered target, the cryogenic THD fuel. Inner and outer integration limits on the above formulae are thus set by the inside edge of the ablator and the ablation front, respectively. In practice, these limits are important only in defining these quantities in the simulations since the use of fitting functions with compact support (i.e., zero outside a bounded region) obviate the need for explicitly defining integral limits.

In the definition of ignition metrics, it is the peak fuel velocity that is of central importance since this directly determines hot spot compressive heating. Due to geometric convergence the maximum fuel velocity, defined[5] as $\sqrt{}$(2×fuel kinetic energy/fuel mass), is generally higher than the maximum ablator center-of-mass velocity, since the fuel is at smaller radius. Surrogacy differences between symcaps and layered shots only slightly modify this relationship. Simulations of both types of capsule[44] show that the peak fuel velocity in a layered shot is 8%–12% higher than the center-of-mass velocity of a *symcap* ablator, with larger differences correlating with larger ablator mass remaining (where the ablator and fuel center-of-masses are separated by a larger distance). This correction, plus an additional +2% correction due to the use of backlighter beams in *ConA* experiments, need to be used when comparing a measured velocity to the 370 μm/ns ignition requirement. Alternatively, the ignition requirement translates to an observed shell velocity of ~330 μm/ns.

The ablator mass measured in a *ConA* experiment includes the surrogate CH payload (ζ) that is $\simeq$6% of the initial *ConA* ablator mass. The equivalent remaining mass fraction on a layered target would then be $(f_M - \zeta)/(1 - \zeta)$, where f_M the mass fraction measured in a *ConA* shot. Thus, if the minimum remaining mass fraction requirement[5] is 9.5%, measured *ConA* mass fractions should not drop below 15%.

B. Analysis

The radiographic analysis technique is based on the fact that critical information in the shell radiograph exists at three distinct length scales. Aggregate quantities of the unablated shell density profile occur at scales of tens of microns while ablated blow-off and backlighter variations exist at scales of hundreds of microns. Features such as material interfaces and shock fronts occur at scale lengths of a few microns that are not visible at current instrument resolutions. An appropriately designed regularization technique can thus separate the unablated density profile from the other variations. It is the intermediate scale length of tens of microns that sets the global dynamics of the implosion and is the focus of this study.

Since the original technique was reported,[19] modifications have been developed to allow the shell thickness and density to be estimated accurately. Originally, it was found that inferring the average shell radius, mass, or ρR accurately was quite insensitive to whether or not the correct instrument resolution was used in the analysis. In contrast, when determining the shell thickness and density the instrument blurring must be accurately represented. The updated analysis uses a maximum entropy deconvolution procedure[63,64] to remove spatial blurring due to the finite imaging slit, temporal blurring due to the camera temporal resolution, and the effect of the two-dimensional camera point spread function which, though mostly narrow, also has a long tail which must be accounted for to accurately determine capsule mass. In a streaked radiograph, this is simply a single two-dimensional deconvolution prior to the analysis. In a sequence of gated images, the temporal blurring must be self-consistently determined from the shell velocity, thus requiring at least two passes at the analysis and a spatial resolution width that changes with time. Though deconvolution can in principle be avoided by using a forward

iterative scheme, in practice, the presence of an unknown background level requires that deconvolution of the spatial blurring portion be performed first in order to accurately determine the background behind the central fiducial wire.

Background subtraction is an important step in the analysis, especially while the laser is on, due to the presence of a hard x-ray signal. Background values are sampled at the outside edge of each radiograph and also under the central fiducial wire—a polynomial fit being performed to interpolate the background levels within the backlit portion of the radiograph. Background subtraction is performed after deconvolution in order that the shadow from the central fiducial wire on the hohlraum provides a good representation of the background in the center of the radiograph. The subtraction is performed at each time step since background levels vary with time, especially near the end of the laser pulse.

The original iterative forward regularization approach has been complemented by a direct Abel inversion technique, which is more intuitive and gives nearly identical results. In this approach, the Abel inverse transform is performed on the logarithm of the data *before* the unknown backlighter profile, $I_0(y)$, is determined. The logarithm converts $I_0(y)$ in Beer's Law from an unknown multiplicative function to an unknown additive function akin to a background level. The inverse Abel transform, which involves a derivative, is a high pass filter that amplifies the localized shell density feature and suppresses the slowly varying backlighter and blow-off profiles. This process of Abel inverting the logarithm of the data reduces the problem of separating $\rho(r)$ (in radius-space) and $I_0(y)$ (in image space) to one of finding a coherent density spike on a low-level background in radius-space, much like identifying a single spectral line. More details of this approach are given in Appendix.

An ambiguity exists in how the ablator opacity (at the backlighter energy) is determined for an ablator comprised of graded dopants. Originally, two methods were described to address this,[19] an exact method and a mean opacity method. In the exact method, the assumed $\rho(r)$ is used to convert the known initial Lagrangian opacity profile $\kappa_\nu(m)$ to an Eulerian opacity profile $\kappa_\nu(r)$ at each time step. This technique is rigorous in that it assigns the appropriate κ_ν to each mass element in $\rho(r)$ (effectively assuming no mixing), though it results in an unblurred $\rho(r)\kappa_\nu(r)$ fit function with sharp discontinuities at the layer interfaces. Fitting this discontinuous function to both synthetic and real data has been found to introduce minor oscillations of the density and thickness. For this reason, the data have largely been analyzed using the mean opacity technique. Here, the average opacity, $\overline{\kappa_\nu}(M)$, of the unablated shell is given by

$$\overline{\kappa_\nu}(M) = \frac{\int_0^a \kappa_\nu(m)\mathrm{d}m}{\int_0^a \mathrm{d}m} = \frac{\int_0^a \kappa_\nu(r)\rho(r)r^2\mathrm{d}r}{\int_0^a \rho(r)r^2\mathrm{d}r}. \quad (6)$$

Both the forward and inverse analysis methods have been tested on synthetic radiographs to establish the accuracy with which each of the observables described above are determined. Fig. 2 shows the synthetic radiograph while

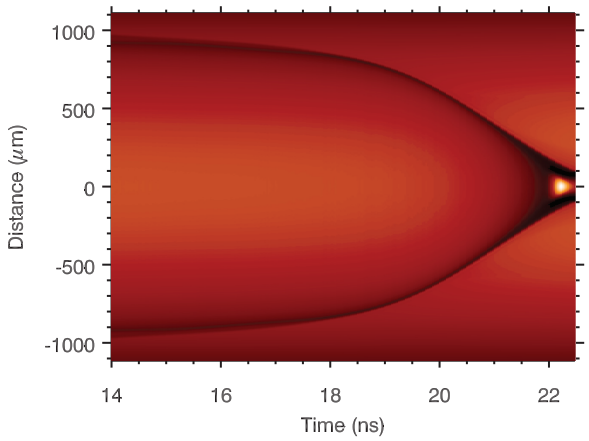

FIG. 2. Simulated radiograph used to perform the test analysis. Radiograph has 50 ps of temporal blurring and 17 μm of spatial blurring.

Fig. 3 shows the fitted profiles at four time steps. Final results are compared in Fig. 4. As can be seen, both the forward iterative and inverse methods give nearly identical results and are in good agreement with values obtained directly from the simulations. Note that late in time, systematic biases in the analyses lead to velocities that are slightly higher than simulations at a given mass remaining and shell thicknesses that are slightly smaller than simulations. As will be shown, both these effects are the opposite of what is observed in the experiments.

IV. SEMI-EMPIRICAL SIMULATIONS

Experimental results are compared to two-dimensional HYDRA[65] simulations of the hohlraum and capsule. These use the "high-flux" hohlraum model[66] with flux-limited electron thermal conduction using a non-local thermodynamic equilibrium (nLTE) atomic physics model with direct configuration accounting (DCA). The hohlraum wall opacity and emissivity is calculated from local thermodynamic equilibrium (LTE) tables for temperatures below 300 eV and an nLTE DCA model at higher temperatures. Selected tabular opacities (OPAL[29] and VISTA[67]) and equations-of-state[68] are used for the ablator and DT fuel. The input laser power is modified to account for backscattered energy and crossbeam energy transfer in the hohlraum plasma.[38,40]

As described in Sec. I A, baseline simulations were found to overestimate measured shock velocities and underestimate the x-ray bang time, implying that capsule ablation pressures are systematically overestimated. This is despite the apparent agreement[38,69] between the simulated and measured x-ray drive. To address this discrepancy, a semi-empirical model was developed,[70] which fits the shock velocity data,[17,18] as well as some of the *ConA* data described in this paper, by an *ad-hoc* reduction in the laser power. Of course matching the capsule dynamics this way had the undesired effect of degrading the previous agreement between the simulated x-ray drive and the measured Dante power.[70]

This fitting approach means that the simulations shown in this paper are not meant to be predictive, or even postdictive, as they already incorporate certain aspects of the

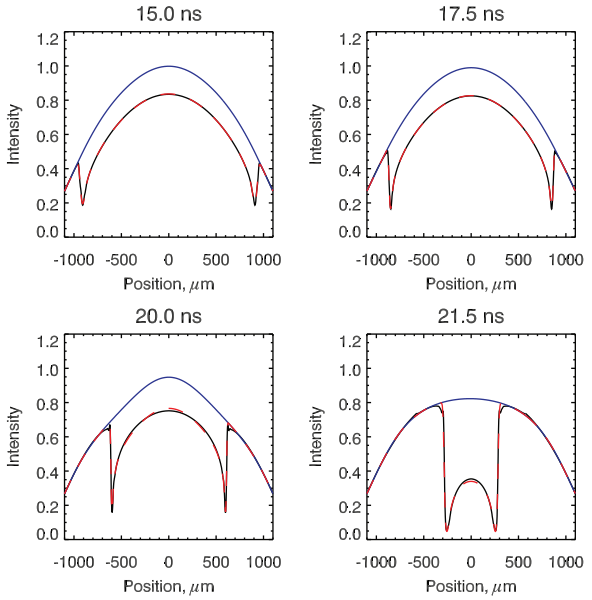

FIG. 3. Simulated x-ray intensity profile at various times (black) along with the best fit from the original regularization analysis (dashed red) and the inferred unattenuated intensity (blue). Gaussian density profiles are assumed throughout. The radiograph, with 50 ps of temporal blurring and 17 μm of spatial blurring, has been temporally and spatially deconvolved prior to analysis.

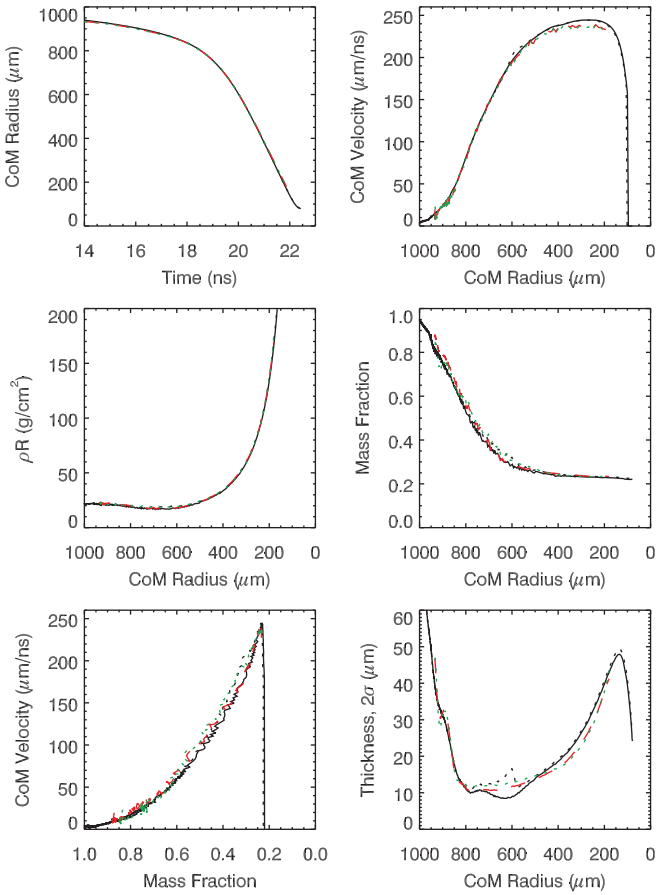

FIG. 4. Comparison of results obtained from analyzing the simulated streak using the previously described forward technique (dashed red) and the new inverse technique (dotted green). Values obtained directly from the simulated density profiles are shown for cases where the ablation front is defined in terms of a radiation temperature cutoff (solid black) and a density cutoff (dotted black). Both forward and inverse radiographic analysis techniques accurately capture the simulated inputs for all parameters.

data to which they are being compared. In particular, *ConA* data were used to determine the final laser "multiplier" on the peak of the pulse. Typically, this was about 85%–87%, meaning that 13%–15% of the peak laser energy was discarded. In the early shots, this value had not been fixed and some of the simulations used 100% multipliers and 92% multipliers (this will be described below). All simulations include individual multipliers that are applied to various features from the foot of the pulse up to the 4th rise. This work discusses only the multiplier that applies to the peak drive portion of the pulse.

Note that though many of the simulations have been effectively re-normalized towards the measured capsule trajectory and bang time, they have not been adjusted to account for other *ConA* parameters, in particular, the shell mass and thickness.

V. RESULTS

Results below are described roughly in the order the shots were taken over the period between 2010 and 2012. This captures the chronology of when surprises were discovered and what design changes were implemented to address the challenges. It also illustrates the way that the simulations were adjusted to try to match the data. The experiments have been divided up into sections according to the peak laser power used. This orders the shots in terms of their broader campaign goals: High power experiments were attempting to maximize velocity, while the lower power extended pulses were used to improve fuel ρR on accompanying layered shots.

Each section has a collection of figures comparing the suite of radiographic data obtained for each shot, giving the time-resolved radius, radially resolved velocity, ρR, mass, and thickness, and the velocity-mass "rocket" curve. The laser power history for each shot, for the backlighter beams as well as the main beams, is also shown. Table III provides an overall summary for each shot, giving essential capsule, hohlraum, and laser parameters along with some neutron and x-ray core emission results.

A. Ge-doped capsules: Commissioning tests and the Rev5 point design

Initial *ConA* shots were taken using the Ge-doped CH "Rev5" point design target,[45] where the "5" refers to the latest revision number of the point design target. Two shots were taken using ~1 MJ of laser energy at ~300 TW peak power (the laser operations limit at the time) to commission the *ConA* platform and to obtain initial measurements of implosion velocity. The first shot (N101218) used a short, high-foot pulse. This pulse was designed to mitigate the problems of LEH condensate on DT layered targets and D_2-filled shock-timing targets.[17,71] The second shot (N101220) used the longer Rev5-type pulse. Note both these pulse shapes were not "shock timed" since available shock velocity data were compromised by LEH condensate.

Subsequent shock timing data, taken using targets with thermally insulating windows to solve the condensate problem,[17] resulted in significant modifications to the foot of the pulse and the timing of the 4th rise. Radiographic images from a *ConA* shot (N110625) incorporating these changes and using a 1.3 MJ, 430 TW pulse are shown in Fig. 5 with sample profile lineouts and fits given in Fig. 6. This shot was the first peak velocity measurement of the shock-timed, Rev5 ignition design and thus represents the first complete assessment of the performance of the point design.

The inferred *ConA* parameters from this shot are shown in Fig. 7 and compared to those from the first two shots. As can be seen in Fig. 7(a), the shock timing modifications implemented on shot N110625 (green) included a pulse with a higher power picket, a longer trough, and a delayed 4th rise compared to the point design. Each of these adjustments push the peak capsule velocity lower. Changing from a pulse that was shock timed in simulations (black and red) to one that was shock timed experimentally thus offset any increase in peak velocity that might have been gained by raising the laser power and energy from 300 to 430 TW and 1.0 to 1.3 MJ, respectively. As a result, all three shots had a peak velocity near 250 μm/ns (Fig. 7(c)). Most importantly, the shock-timed Rev5 ignition point design only reached 75% of the velocity goal of 330 μm/ns, considerably lower than expected.

Accompanying data in Fig. 7 illustrate how this observed velocity deficit manifests itself in the suite of radiographic data. The remaining mass is above the Rev5 design limit of 15% (Fig. 7(e)), consistent with an overall reduced drive on the capsule. Put together, this lower velocity and higher mass can be seen on the velocity-mass rocket curve to fall well short of the goal, diverging from the rocket curve too early (Fig. 7(f)).

The semi-empirical simulations shown in these plots all implement laser multipliers on the foot of the pulse to reduce the laser energy, so that the simulated shock velocity matches accompanying shock timing data (see Sec. IV). However, the multiplier on the peak of the pulse is kept at 100% in these simulations. As can be seen, this results in the simulated implosions converging faster, earlier, and with less remaining mass than observed. Importantly, it can also be seen that the simulated point design now only reaches 300 μm/ns—10% below the ignition velocity. This reduction is due to the changes in pulse shape (multipliers) required to match the shock timing data.

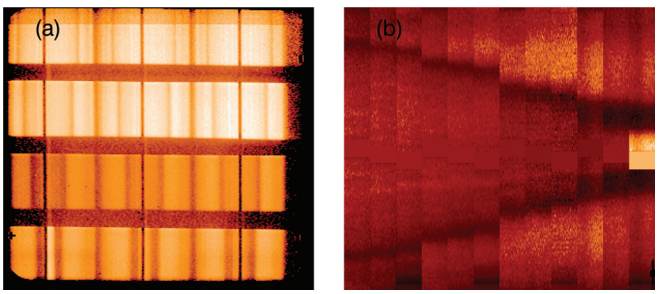

FIG. 5. Measured radiograph from the Rev5 Ge-doped CH shot, N110625. (a) Raw data on four strips. Each strip, separated by ~350 ps, records 3 images separated by ~70 ps. The center of each image is obscured by the shadow of the tungsten fiducial wire. (b) Stitching the images together sequentially in time produces a "streak," with time going from left to right. Note the slightly brighter spot in the streak, converging from the bottom left, is likely a thin spot in the ablator.

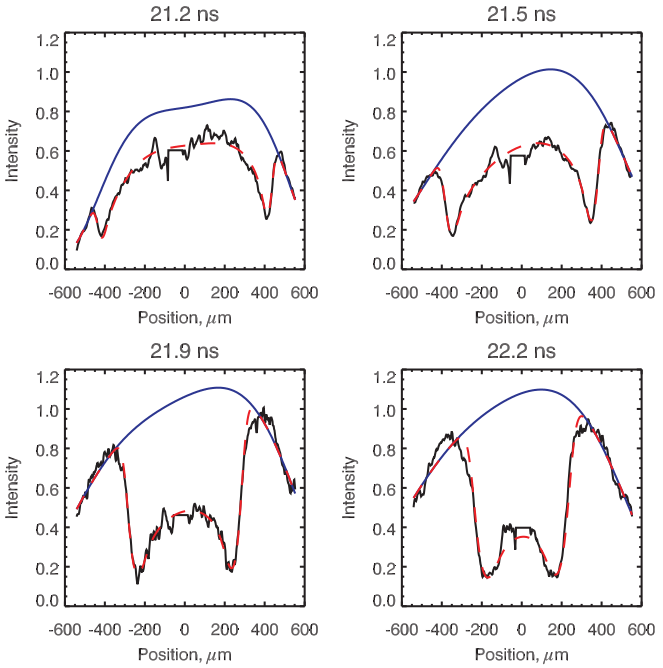

FIG. 6. Radiographic lineouts from Shot N110625 (black) showing the best forward fit to the data (dashed red) and the inferred unattenuated backlighter intensity (blue).

Measured shell thicknesses are larger than simulated values for both the longer foot, Rev5-type pulses, whether shock-timed or not. At least some of this discrepancy is due to the lower peak drive on the capsule in the experiment, which reduces the density of the ablator. Better agreement exists between simulation and experiment for the high foot pulse. Generally, it is desirable to have a higher density (thinner) ablator to maximize the pressure and confinement of the fuel at stagnation.

B. Si-doped capsules: >400 TW peak laser power and 1.2–1.5 MJ laser energy

Different campaigns were conducted to investigate how various laser and target changes could improve ablator performance. The effects of changing the ablator dopant from Ge to Si as well as altering the length and rise time of the main pulse were investigated. Several shots were taken to measure the shell dynamics throughout the acceleration phase, attempting to identify the origin of the observed performance degradations. Shots used peak laser powers of 420–430 TW, the facility limit at the time.

1. Tests of Ge vs Si dopant

With the Ge-doped point design showing velocities 25% below the ignition goal and thus needing unanticipated design modifications, one modest change involved altering the dopant material. Replacing Ge dopant with Si was hypothesized to increase velocity since the lower Z dopant allows more x-ray drive to reach the ablation front. Design

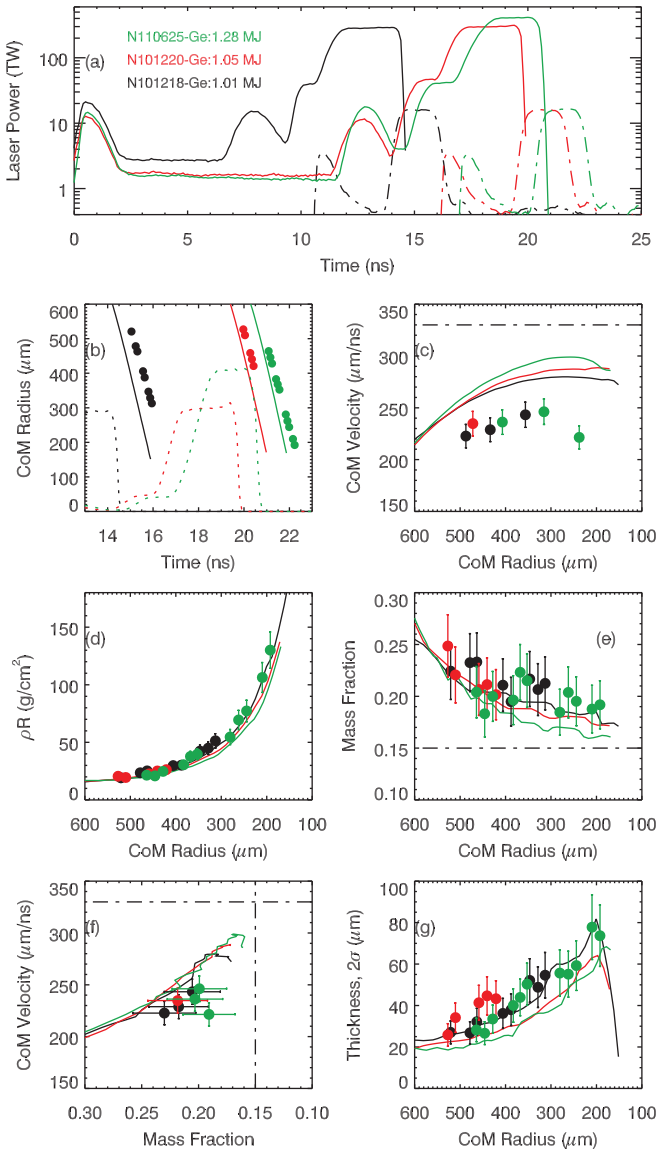

FIG. 7. Data from 3 ConA shots. (a) Laser power at LEH (solid lines) and backlighter power (dotted-dashed lines) versus time. Data extracted from radiograph: (b) Ablator center-of-mass radius versus time, also showing the laser pulse (dotted) for reference, (c) Ablator center-of-mass velocity versus radius, (d) Ablator ρR versus radius, (e) Ablator mass remaining fraction versus radius, (f) "Rocket curve" of velocity versus mass, and (g) Shell thickness versus radius. Data are given by solid points with error bars. Simulations are shown with solid lines. For these shots, the simulations used laser multipliers to roughly account for shock timing data but use a 100% multiplier on the peak of the pulse. Ignition requirements of 330 μm/ns in shell velocity and 14.5% total remaining mass are marked on the velocity and mass axes with dashed-dotted lines. Note that a timing error resulted in only partial data being acquired on N101220. Color legend is given in (a).

calculations indicated that it was possible to set the Si dopant concentration at a level that generated increased ablation pressure without adversely pre-heating the fuel.

The dopant layers in these targets, located towards the inside of the shell, begin to be ablated when there is $\lesssim$30% ablator mass remaining. This occurs near the end of the laser pulse when the capsule is inside a radius of $\lesssim$700 μm and still at only 60%–70% of peak velocity. The benefits of changing the dopant material should thus be gained entirely at the end of, and after, the laser pulse. The simulations shown in Fig. 8(c) illustrate how replacing Ge with Si was expected to bring the simulated shell velocity back up to ignition requirements, recovering the losses incurred from the shock timing adjustments.

A direct experimental comparison of Ge- and Si-doped targets was performed by driving both with similar laser pulses. As can be seen in Fig. 8, the Si-doped shots (N110627 and N110630) had peak velocities of $\sim$280-290 μm/ns, a $>$10% improvement over the Ge-doped shot (N110625) (the two Si-doped shots had 200 ps different pulse lengths but did not exhibit significant velocity differences). This velocity increase was consistent with the $\sim$200 ps earlier bang times observed with the Si-doped targets, indicating a higher average ablation pressure using Si dopant. Consistent with the increased velocities, the remaining ablator mass was lower in the Si-doped than the Ge-doped targets, dropping below the ignition minimum of 15%.

Due to manufacturing differences, the Si-doped targets had slightly lower densities (even of the pure CH), larger inner radii, and larger thicknesses (see Table I). These were calculated to have caused about half of the observed increase in velocity, primarily from the larger inner radii. Accounting for these target differences indicates that the velocity improvement due to dopant effects alone was +5%–7% when comparing 2% Si-doped ablators and 1% Ge-doped ablators, slightly larger than expected from simulations.

A noticeable feature of both the Ge-doped and Si-doped capsule implosions is that the velocity peaks at a radius $>$300 μm whereas simulations indicate that peak velocity should occur at $\sim$250 μm. A fuel layer beginning to decelerate at a larger radius has a larger enclosed volume upon which work must be done and thus results in a lower final stagnation pressure. Examining the density profiles in these data indicate that the velocity of the inside edge of the ablator (which would be most closely related to the fuel velocity) is still accelerating inside 300 μm, and it is rather the outside edge of the ablator that is responsible for the average deceleration of the center-of-mass. This rules out the possibility that an anomalously early shock wave returning from the capsule center is causing the early deceleration.

Premature deceleration of the ablation front at the end of the implosion is likely due to Rayleigh-Taylor instability growth in the unpolished capsules used in all these initial shots. Subsequent shots with polished capsules showed deceleration beginning at smaller radii, indicating that more instability growth was present in these preliminary experiments. It is possible that performing the Si vs Ge test in unpolished capsules may have exaggerated the differences between the two materials since mix of the dopant layers into the outer pure CH regions could have caused ablation of doped regions earlier in the pulse. Nevertheless, given the apparent improvement observed in Si vs Ge-doped targets, all subsequent shots in this study used Si-doped CH.

2. Extended pulse length to reduce coasting

Ignition designs originally set the main laser pulse to turn off once the capsule radius reached about half the initial radius ($\sim$500 μm). Because capsule trajectories were slower

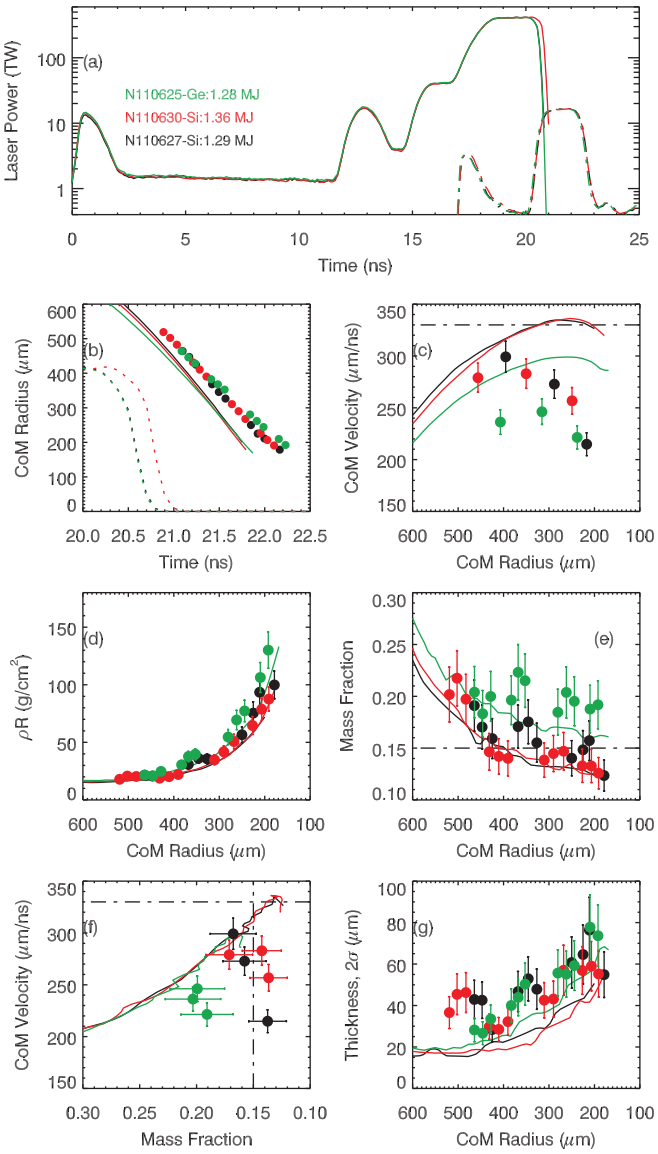

FIG. 8. Data showing the comparison of Si-doped and Ge-doped implosions. Laser pulses for N110625 (Ge) (green) and N110627 (Si) (red, black) were nearly identical and overlap each other. Si-doped capsules have a higher peak velocity and lower remaining mass than Ge-doped capsules indicating a higher ablation pressure is achieved using the lower-*Z* dopant. Simulations used laser multipliers to fit shock timing data in the foot of the pulse but use a 100% multiplier on the peak of the pulse. The apparent early deceleration of the Si-doped capsules is due to deceleration at the ablation front, rather than the inner edge of the capsule, and is likely due to hydrodynamic growth in these unpolished capsules.

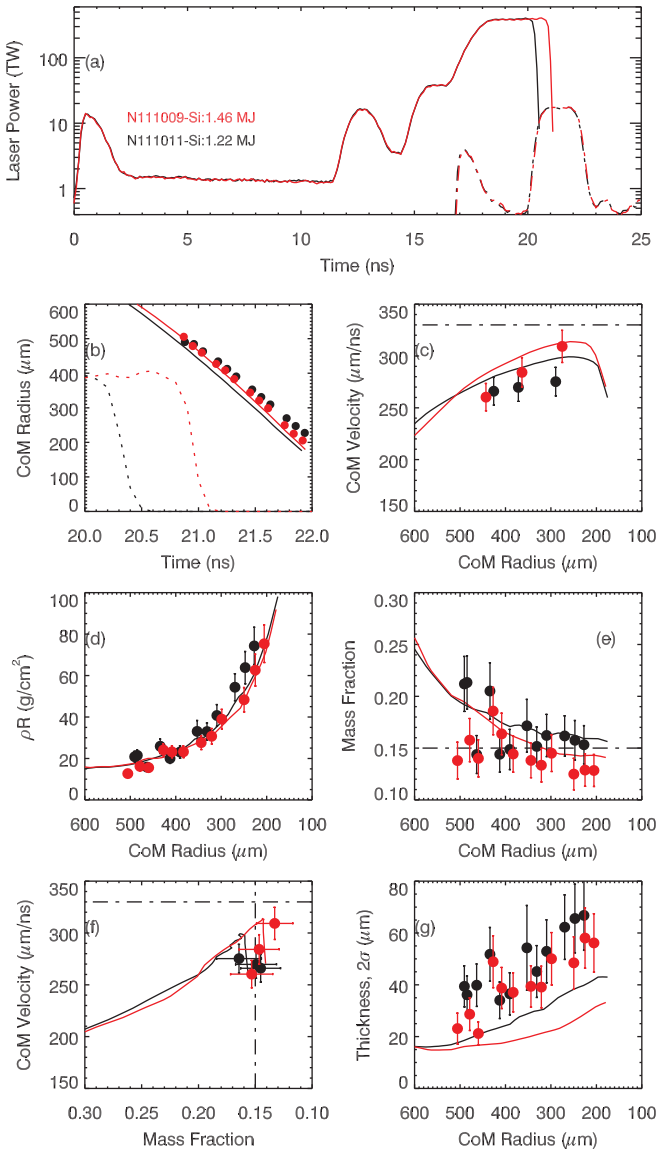

FIG. 9. Data showing the ~10% improvement in shell velocity achieved by increasing the peak power duration by 600 ps. The increased acceleration using the extended pulse is apparent in radius and velocity records, along with the reduced ablator mass and thickness. Simulations used laser multipliers to fit shock timing data in the foot of the pulse and an 87% multiplier on the peak of the pulse to attempt to bring the simulations into better agreement with these data.

and later than expected, the capsule radius was at only 600-700 μm when the laser turned off. Lengthening the laser pulse, and thus reducing the length of this "coasting" regime, was hypothesized to be a relatively simple way to increase the capsule velocity. The primary penalty for this strategy is the increase in optics damage from the increased laser energy.

To test this hypothesis, two shots were performed, one driven by a standard length pulse (N111011), the other driven by a pulse that was 600 ps longer (N111009). Both pulses had the same peak power. The foot of these pulses was set by shock timing of Si-doped capsules, giving a slightly different pulse shape to that in Sec. V B 1 where the pulse was set by shock timing of Ge-doped capsules. The hohlraum in these shots was changed to a shorter wider design, having an inner diameter and length of 5.75 mm and 9.425 mm rather than the original 5.44 mm and 10.01 mm. This design change,[44] motivated by a separate symmetry campaign, attempted to reduce the demands on cross-beam energy transfer by allowing more heating of the hohlraum waist by the outer cone beams. The LEH diameter was kept the same as in previous shots.

Increasing the pulse length by 600 ps raised the measured peak velocity from 275 μm/ns to 305 μm/ns, a ~10% improvement that reached ~93% of the ignition requirement. Separation of the two trajectories, apparent in the data record (Fig. 9(b)), begins after the end of the longer pulse,

demonstrating the several hundred picosecond time delay between laser and capsule drives. The longer pulse resulted in radial trajectories converging earlier, a 120 ps earlier x-ray bang time, and a ~60% higher DD neutron yield of 7.4×10^{11}, the highest *ConA* yield achieved as of this writing (see Table III). As can be seen in Fig. 9, the mass remaining was reduced correspondingly, as was the thickness of the shell, all indicative of the higher ablative drive late in time achieved using the longer pulse.

Although changing to a Si dopant and extending the laser pulse significantly increased the drive at the end of the implosion over the Ge-doped case, capsule velocities were still below those expected from nominal simulations, with the measured velocity corresponding to a peak power deficit of ~13%-15%. The origin of this large discrepancy was, and remains, unknown though it is likely in part due to an overestimate of the hohlraum x-ray conversion efficiency.

3. Detailed history of behavior from before to after peak drive

ConA measurements were originally designed to examine the end state of the acceleration phase, after the laser pulse turned off and just prior to bang time. Given that shock timing measurements operate only up to the rise of the main laser pulse, this meant that there was no diagnostic of the capsule response throughout peak laser power.

In the NIF designs, little attention was given to this part of the implosion. Once shocks were timed, the capsule would be driven by a flat-top peak laser power to maximize the capsule acceleration regardless of higher order capsule dynamics, such as might be caused by additional shocks or an unsteady ablation pressure. Given the growing experimental anomalies, in particular, the unexpectedly low neutron yields,[70] and fuel areal densities[22] in companion DT implosions, diagnosing the capsule response over its complete history became an important goal.

A related goal was to examine the sensitivity of implosion dynamics to the main pulse rise time. Shorter rise times were expected to give faster implosions but could potentially compromise fuel adiabats since the 4th shock is stronger and more difficult to time; in contrast, slower rise times were expected to produce lower peak velocities but should achieve lower fuel adiabats with less stringent demands on 4th shock timing.[13] A set of *ConA* experiments were performed to examine how the rise duration affected the shell velocity and thickness throughout the acceleration phase. These tests used the standard 2 ns rise time, as well as slower (3 ns) and faster (1 ns) rises.

Eight shots were used to characterize the implosion dynamics before, during, and after the main pulse. Because the backlighter pulse length was limited to ~2.4 ns, only select time windows could be studied for each pulse type. Target design changes from previous shots were minimal and included widening the slots in the hohlraum and offsetting the pointing of backlighter quads (see Sec. II E) to provide a wider field of view. This new type of target is referred to as a *ConAw* target in Table II. One change, inherited from the symmetry campaign, was the use of a larger LEH diameter of 3.373 mm (rather than 3.101 mm) designed to reduce hypothesized clipping at the LEH.

The first group of shots (Fig. 11) examined the implosion history of the standard, 2 ns rise pulse. Three shots (N111220.2, N111218, and N111219) were used to map out the capsule behavior starting after the 2nd shock, the regime of shock timing measurements, and continuing to the end of the laser pulse, the realm of previous *ConA* measurements. Camera timings for each shot were set to provide complete and overlapping coverage of a ~7 ns region. Note that the earliest time window measurement (N111220.2) examining the period around 2nd and 3rd shocks, used a main pulse with a 1 ns rise which did not affect the measurement (this was done to provide an initial estimate of the bang time and stagnation performance for this shorter rise time). A fourth shot examined the implosion dynamics towards the end of the 3 ns rise time pulse.

Slight changes were made to the foot of the pulse, raising and delaying the 2nd pulse, and bringing forward the 3rd pulse, in order to reduce the large gap between these pulses (see, e.g., Fig. 9(a)) arising from results of the shock timing measurements. Allowing the ablator to release significantly between successive shocks could raise the ablator adiabat, lowering its density, potentially causing the thicker shell observed late in time (see, e.g., Fig. 9(g)). This would also make the fuel-ablator interface more unstable to hydrodynamic instability growth. For facility reasons, these pulse shape changes had to be made by dead reckoning. Later measurements on the shock timing platform showed that the gap had been closed too much and would have caused the 2nd and 3rd shocks to coalesce in a fuel layer. In the subsequent four shots, the pulses were separated to produce the desired shock timing.

A time sequence of radiographs is shown in Fig. 10. Analysis of the first four shots (one from the slower rise pulse) is shown in Fig. 11 and compared to simulations, which have been degraded by 15% (an 85% laser multiplier) in the peak. The usual multipliers have been used throughout the foot of the pulse to account for shock timing. The data show reasonable agreement in radius and velocity (by design), as well as mass and ρR. The observed shell thickness was in agreement with simulations through 2nd and 3rd shock compression but begins to deviate after break-out of the 4th shock (at a radius of ~900 μm) where a larger-than-expected thickness was observed. The largest discrepancy

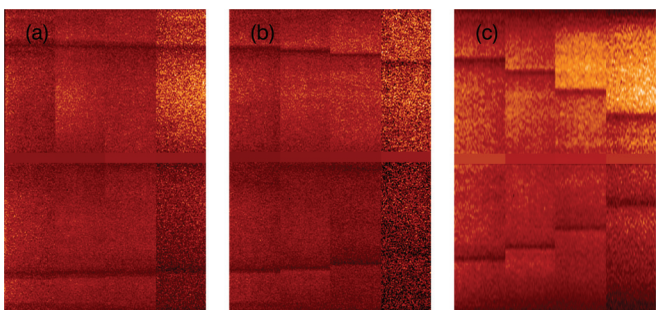

FIG. 10. Radiographs from 3 different shots ordered sequentially in time. These images span radii from ~940-380 μm and a time window of ~7 ns.

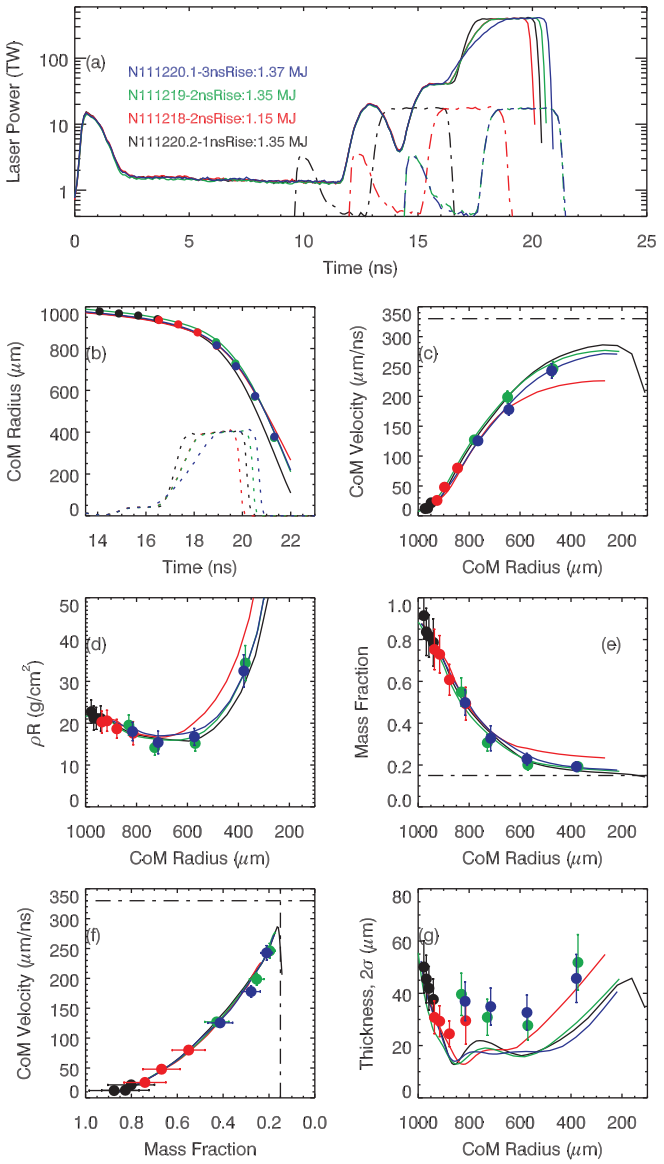

FIG. 11. A study of implosion dynamics before, during, and after the main laser pulse. Measurements on each shot covered a ~2.4 ns window set by the backlighter pulse length. To cover the period from the 2nd shock to the end of the main pulse, camera timings were shifted from shot to shot, building a composite history of a characteristic 2 ns rise implosion using shots N111220.2, N111218, and N111219. Note that though N111220.2 used a 1 ns rise pulse and N111218 used a shorter duration pulse, radiographic measurements were performed before these features occurred, and thus were still characteristic of the "standard" 2 ns rise pulse. Shot N111220.1 was the first shot to use a 3 ns rise pulse. Simulations use shock timing multipliers as well as an 85% multiplier in the peak.

with simulated thickness, however, still occurs at the end of the implosion where it had been observed previously.

To illustrate the discrepancy in shell thickness, the measured and simulated opacity-density, $\kappa_\nu(r)\rho(r)$, profiles are compared in Fig. 12. The first figure shows the profile around the time of the 2nd shock and has two peaks. The inner peak arises from the higher opacity of the inner doped layers; the outer peak comes from the higher density shocked pure CH being driven inwards. This profile is in relatively good agreement with the simulations, which have been adjusted to match the shock timing data. Late in time, there is only a single peak, corresponding to the high density

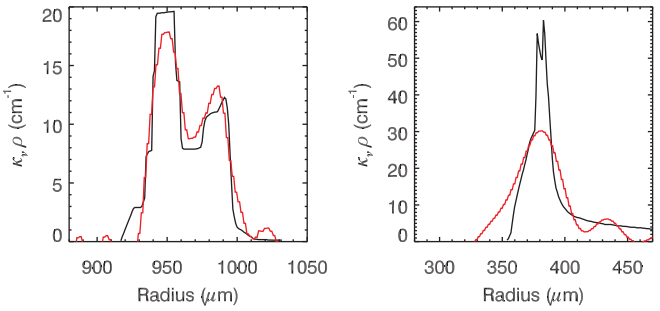

FIG. 12. Comparison of measured (red) and simulated (black) density-opacity, $\kappa_\nu(r)\rho(r)$, profiles around the time of the 2nd shock (left) and approaching peak velocity (right). At the early time, the inner peak corresponds to the doped region of the shell while the outer peak corresponds to the incoming shock wave in pure CH. Late in time, the observed shell is thicker than simulations.

doped region since the outer layer of pure CH has been removed by ablation. This $\kappa_\nu(r)\rho(r)$ profile is considerably thicker than the simulated profile.

These initial results indicated that there was little difference in shell thickness between the 1 ns and 2 ns pulse rise times and also that there was little difference in maximum velocity between the two rise times. Though the shorter (2 ns) rise accelerated the capsule at a larger radius than did longer (3 ns) rise, as expected, the final velocity achieved was, unexpectedly, almost identical.

To further examine this behavior, 4 shots were performed directly comparing capsule behavior of the fast (1 ns) rise and the slow (3 ns) rise soon after 4th shock break-out and around peak velocity. As mentioned above, these fast and slow pulse shapes had a gap between 2nd and 3rd pulses that was a few hundred picoseconds larger than on the first 4 shots. To perform a clear comparison, the total energy and peak power of the slow and fast rise pulses were kept nearly identical.

As shown in Fig. 13, the fast rise pulse resulted in a peak velocity that was slightly lower than the slow rise pulse. This is the opposite of what was expected both from simulations and from simple geometric reasoning: since the faster rise generates a higher hohlraum temperature when the capsule is at a larger radius, the greater surface area should result in more work being done on the capsule. That the opposite occurs indicates that the slower rise pulse is more efficient at converting laser energy to capsule kinetic energy. Observed laser backscatter losses do not account for this difference, suggesting that there is an unseen loss mechanism that is worse in the fast rise than in the slow.

Peak velocities were ~20 μm/ns below those expected from earlier measurements using a smaller LEH diameter, consistent with greater LEH losses from the larger LEH. The lack of evidence for beam clipping and this reduction in peak velocity meant that all subsequent shots would revert to the small LEH design.

Up to the 4th rise, shell thicknesses were close to those simulated, becoming considerably larger late in time. Some of these differences appear to be due to higher order deviations in the drive history that are not captured in the simulations by the flat multiplier on the peak of the laser pulse.

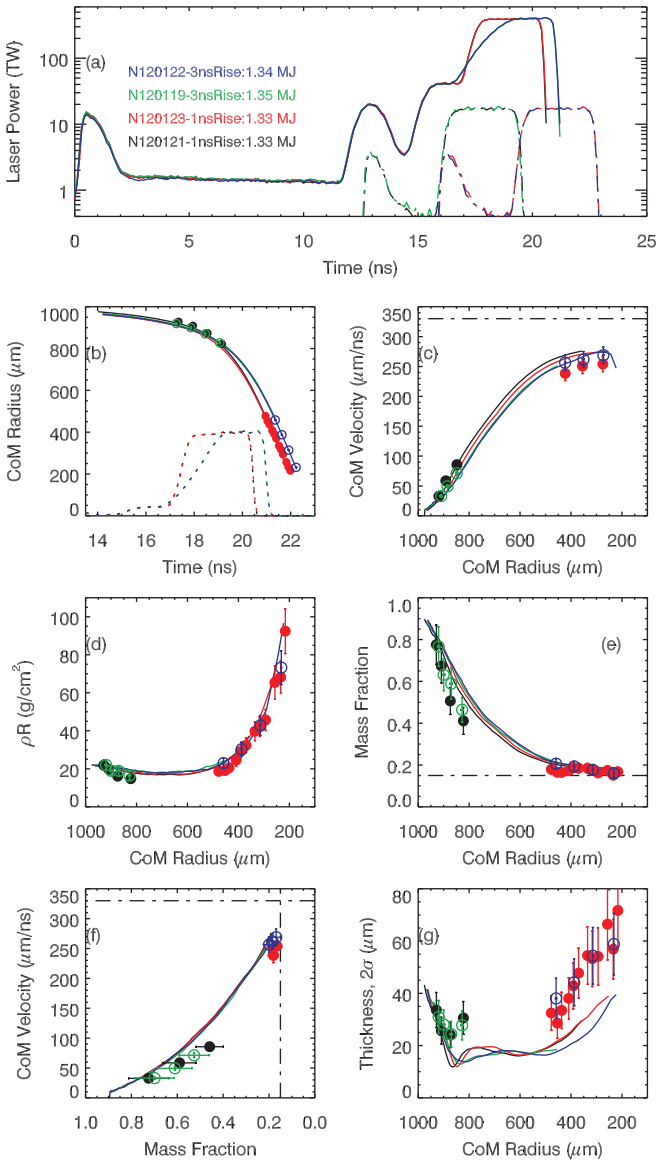

FIG. 13. A detailed comparison of shell behavior around the time of 4th shock break-out and near peak velocity for the fast (1 ns) and slow (3 ns) rise pulses. Pulses for both 1 ns shots (red and black) and 3 ns shots (blue and green) were nearly identical. Slight differences in simulated results within each pair are mainly due to target variations. Unexpectedly, the fast rise pulse resulted in a velocity that was slower than the slow rise pulse (both rise times have the same peak power and laser energy). This suggests that the slow rise is more efficient at converting laser energy to capsule kinetic energy. Simulations here have an 87% multiplier on the peak.

Though the simulated trajectory, by design, approximates the measured trajectory, a closer look indicates that there are subtle differences. In particular, the measured acceleration is larger early in the main pulse and smaller late in the pulse. Properly capturing these higher order dynamics is an ongoing effort but initial indications are that exactly matching the radial trajectory results in a much closer match to the shell thickness.

C. 330-390 TW peak power, "low coast" pulses

In evaluating which pulse shape changes might improve DT capsule performance, raising peak power in order to increase capsule velocity appeared to be a clear way to boost the anomalously[70] low neutron yields. A similar benefit was expected from using the higher laser-to-x-ray conversion efficiency of uranium hohlraums: when compared to gold hohlraums driven by identical pulses at ~420 TW peak power, indirect evidence had shown that uranium hohlraums raise peak capsule velocity by ~4%.[44] However, the first attempt to drive a DT capsule in a uranium hohlraum at 420 TW peak power resulted in a significant yield and ion temperature *decrease*, indicative of ablator-fuel mix into the hot spot. This was the first obvious indication of the presence of a mix cliff in the experimental data, where a steep drop in neutron yield indicated the penetration of higher-Z material into the hot spot. This suggested that implosions with thicker ablators would likely be necessary in order to benefit from higher hohlraum drive. Until these targets could be built and shock tuned, other experimental changes were explored.

Effort was then focused on longer pulse lengths. Lengthening the pulse by 600 ps had already been shown (see Sec. V B 2) to increase peak velocity by ~10%, generating the highest velocity and neutron yield observed in *ConA* experiments to date. Longer pulses were conjectured to raise fuel ρR's on DT layered implosions (which were at 67% of ignition requirements[22]) by maintaining capsule acceleration late into the implosion and thus keeping the dense fuel from releasing before stagnation. This fuel ρR improvement was observed in a THD implosion (see Sec. V D).

Several shots were performed to investigate implosion performance using pulses with a reduced "coasting" phase—the period when the laser is off but the capsule has yet to reach maximum convergence. Traditional designs required the laser to be on until the capsule reached ~50% of its initial radius. As mentioned in Sec. V B 2, the unexpectedly slow capsules meant that coasting would actually begin at 60%–70% of the initial radius. To significantly reduce coasting, the laser pulse length was extended until the capsule had reached ~30% of its initial radius. Additionally, the need to avoid deleterious mix on DT implosions (which, by this time, had been inferred on several layered shots) meant that the *ConA* experiments described hereafter would all use peak laser powers in the range of 330–390 TW.

In addition to testing the effect of a longer pulse, shots were conducted to explore the effect of using different dopant concentrations and distributions, as well as the first test of a thicker ablator.

1. An initial test of the "low-coast" pulses

A single shot was used to assess the effect of the new "low-coast" pulse compared to the traditional "coasting" pulses described earlier. Because of the need to reduce peak laser power (to avoid the dramatic drop in performance seen in DT implosions) and the switch to uranium hohlraums, a clean comparison between the two pulse shapes could not be made. Instead, simulations were used to set the peak power to a level (~330 TW) that would achieve a similar peak velocity to that observed on the earlier coasting, ~420 TW shot (N120122). This new pulse shape had a lower power but used ~100 kJ more laser energy (see Fig. 14(a)). Both pulse shapes had a similar foot and used the slower ("3 ns") slope-

of-rise on the main pulse. Note that the slope-of-rise is specified in terms of the rise time for a pulse which peaks at 420 TW; thus the 330 TW pulse actually had a shorter rise time.

The resulting implosion data are shown in Fig. 14. Trajectories, peak capsule velocities, and remaining masses were nearly identical (~265 μm/ns). Although this similarity between the shots was by design, it did indicate that the semi-empirical simulation model can predict implosions with fairly large changes in pulse shape and hohlraum design. The only observable that was significantly different between the two shots was the thickness of the shell, with the low-coast pulse resulting in a thinner shell.

On earlier shots, the persistent observation of a thicker-than-expected shell suggested several possible mechanisms: (a) The drive pressure was lower than expected late in time, (b) the ablator was stiffer than given by the current equation-of-state model[31] from 1-10 g/cm^3, or (c) hydrodynamic instabilities were causing break-up of the shell. The ability of the longer pulse to compress the shell more late in time hints that not all the shell thickening was due to hydrodynamic instability since increasing the late-time drive would tend to break the shell apart even more.

Extending the laser pulse at lower power did result in an improvement in fuel ρR's of DT implosions. The resulting higher neutron downscattered ratio was also observed in the first *ConA* measurement on a layered target, as will be described in Sec. V D.

2. Change of dopant concentration and distribution and the effect on inferred hydrodynamic mix

The degradation of neutron yield and temperature observed on several layered shots was taken as an indication that ablator material was penetrating into the hot spot. This could be caused by hydrodynamic instabilities seeded at (i) the fuel-ablator interface, (ii) any of the four internal interfaces between doped regions of the graded-doped CH ablator, or (iii) the ablation front. As shown below, experiments varying the dopant concentration or distribution, which would mitigate the first two sources of instability at the expense of the third, appeared to degrade neutron performance even further. This suggested that the ablation front instability was dominant.

Instabilities seeded at the fuel-ablator interface should be reduced by using a higher dopant concentration. This decreases the level of pre-heat reaching the inner ablator region, raising the CH density (and thus the Atwood Number) at the fuel-ablator boundary, and making for a more stable interface. However, during ablation of the doped region, a higher dopant concentration leads to higher opacities and thus a steeper, less stable ablation front. Higher dopant concentrations thus trade-off a more stable ablator-fuel interface for a less stable ablation front.

Similarly, a uniformly doped ablator eliminates the unstable internal interfaces of the graded doped design at the expense of increasing growth at the ablation front. Distributing the dopant throughout the ablator creates a steeper ablation front throughout the implosion.

Three shots were performed to directly compare the ablation performance using the standard, "1×," graded

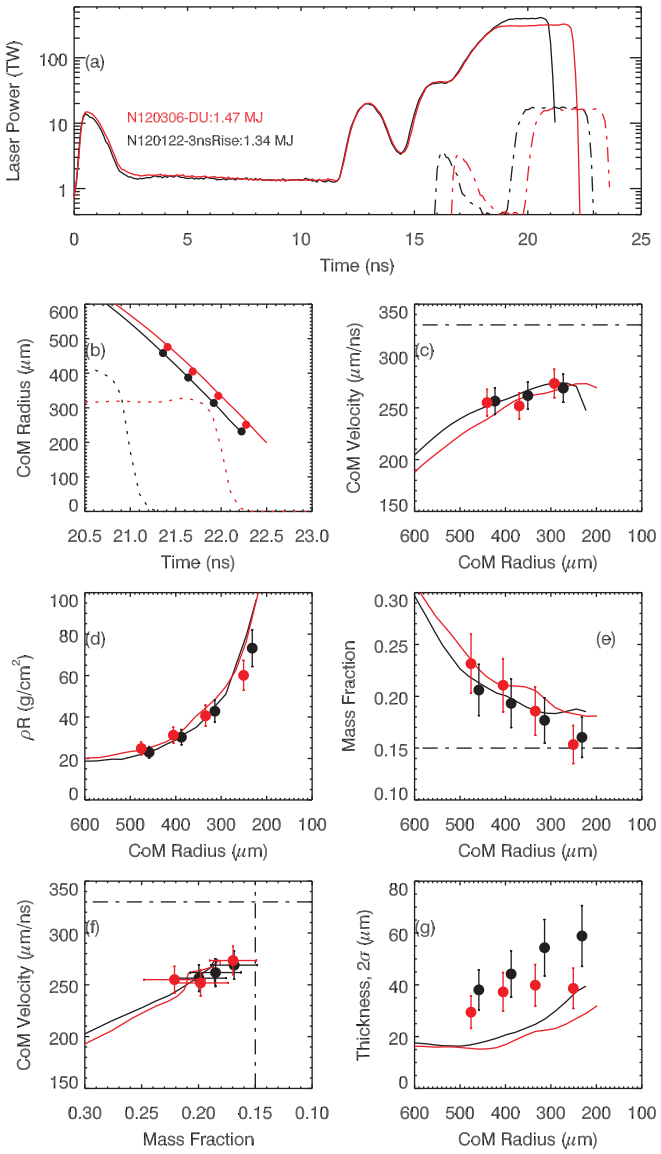

FIG. 14. Comparison of the performance of an implosion using a longer, lower power (~340 TW) laser pulse with a uranium hohlraum to a previous shot using the shorter, higher power (~420 TW) pulse in a gold hohlraum. Both shots have a similar foot and slope-of-rise. The value of the lower peak power was designed to produce the same peak velocity capsule, taking into account the longer pulse and different hohlraum material. Radius, velocity, and mass appear close to simulations using an 87% multiplier on the peak power. The lengthened pulse reduced shell thickness late in time.

doped design, which has a 1-2-1% dopant concentration profile (N120324), a 2× graded doped design having a 2-4-2% dopant profile (N120408), and a uniform dopant profile having 2% Si throughout (N120421). Table I gives the details of each CH layer density and thickness.

The two graded doped targets were shot with uranium hohlraums and nearly identical laser pulses with a peak power of 330-340 TW. The uniform doped target had a gold hohlraum and different laser pulse: the foot was adjusted to compensate for the ablation of doped material early in the pulse, and the peak of the pulse was raised to ~370 TW to compensate for the lower x-ray conversion efficiency of gold versus uranium. No shock timing had been performed on the uniformly doped target, and thus the foot changes were made

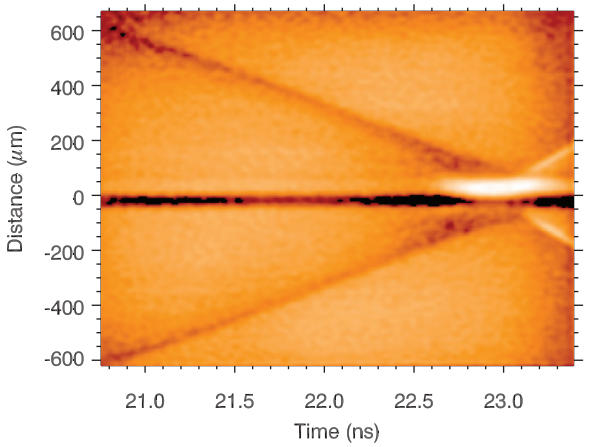

FIG. 15. Streaked radiograph from shot N120408 showing spatial and temporal scales. The central wire provides a background reference. X-ray emission from the stagnating core is visible at ~22.9 ns. At later times, the radiating, outgoing blast wave is apparent.

by calculation alone. All three shots used a 3 ns slope-of-rise on the main pulse.[72]

The radiography data were recorded on a streaked rather than gated camera (Fig. 15). Data points for radius, mass, ρR, and thickness were recorded every 80–90 ps, with each time step being the average of the analysis of two sequential lineouts. Velocity points were obtained by taking linear derivatives of ~4 sequential radius points in order to reduce errors in the derivatives arising from warping and noise in the camera.

Radiography results are shown in Fig. 16. The peak velocity of the graded doped capsules were both ~260 μm/ns, comparable to data obtained on a similar shot using the gated camera (N120306), with the uniformly doped shot having a few percent lower velocity. Masses were also comparable among the three shots, as expected. This was an important test of analysis systematics since there was a 20%–40% difference in optical depth for the 2× versus 1× dopant concentrations. The shell thickness was slightly larger for the 1× versus the 2× graded dopant, consistent with reduced pre-heat in the more heavily doped capsule allowing for greater compression of the ablator.

It is not clear why the ablator mass continues to decrease when the capsule is inside ~300 μm. This behavior was also seen in Sec. V C 1 using the gated camera but was not observed in earlier data or in synthetic data tests. This feature could be significant since the additional decrease causes the mass to drop below the ignition requirement and could explain why significant mix is being observed in the DT implosions. At present, no clear physical mechanism or experimental systematic explains this behavior.

Though the 1× doped ablator was thicker than the 2× doped shell, the yield and ion temperature of the 2× graded doped capsule (2.7×10^{11} and 2.29 keV) were noticeably smaller than that for the 1× graded doped capsule (5.0×10^{11} and 2.45 keV), suggesting that the 2× doped target was more unstable. Increasing the dopant concentration, which improves stability of the inside surface of the ablator at the expense of reduced stability at the ablation front, thus

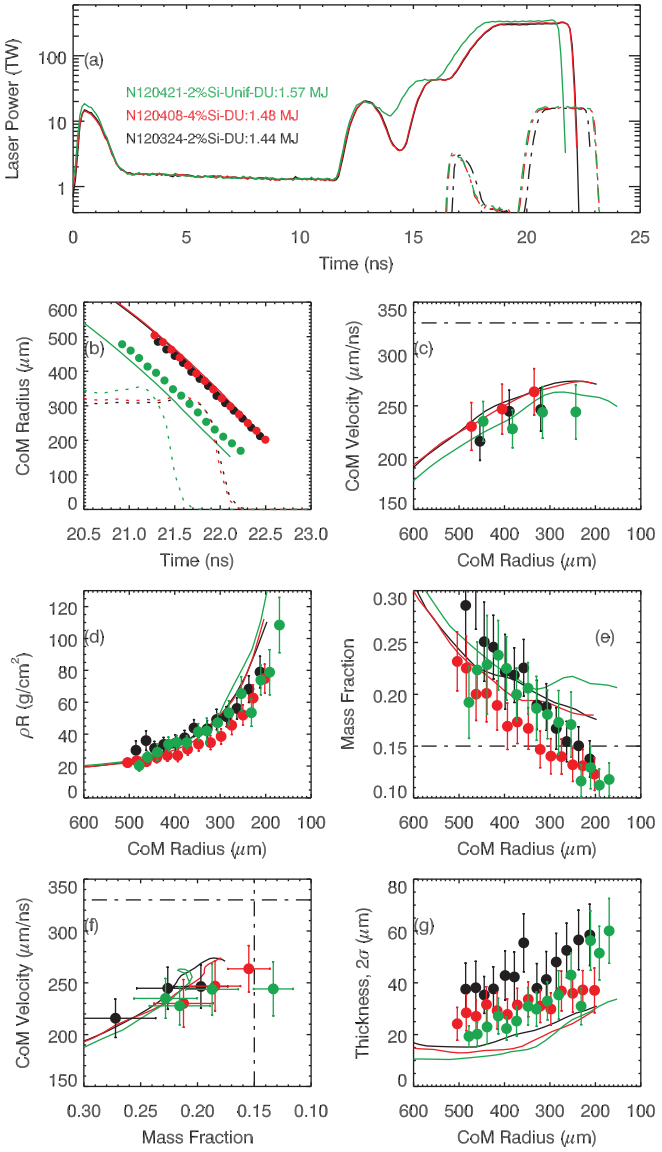

FIG. 16. Comparison of shell dynamics to different dopant concentrations and distributions. Data were recorded on a streak camera. By design, the velocity and mass of these shots were similar. The shell thickness of data using the 2× graded dopant (N120408) was slightly smaller than that for the standard graded dopant concentration (N120324), indicating a higher shell density was achieved with more dopant.

resulted in degraded performance. This indicated that, in the performance of the core, instabilities originating at the ablation front dominated those originating at the fuel-ablator interface. This conclusion was supported by DT layered experiments.

Strikingly, the 2% uniformly doped capsule generated the lowest neutron yield (0.9×10^{11}) and ion temperature (1.50 keV) of any *ConA* capsule to date. This indicated the presence of significantly more instability growth than in the graded doped targets. The presence of dopant in the outer parts of the ablator indicated that much of this additional growth occurred when the mass remaining was >30%. The fact that this capsule did not have a fuel layer or any internal layers meant that all the instability growth originated at the ablation front. This further confirms the inference that the

ablation front instability is a primary concern in these implosions.

These shots demonstrate that ablation front instabilities in the more heavily doped capsules significantly affect stagnation performance of *ConA* capsules. These instabilities produce features at length scales below the resolution of this diagnostic and produce only subtle differences observable in the radiographic data. Nevertheless, the inference from neutron diagnostics is that more dopant degrades implosion performance largely through the destabilizing effect on the ablation front.

3. Improved performance with a thicker shell

One method for reducing the penetration of hydrodynamic mix into the central hot spot from the ablation front is to use a thicker ablator. This requires higher laser powers to achieve comparable velocities to that for a thinner, less massive shell. Though this increases the mass ablation rate, the net result is a larger final mass.[39] This is expected to be more stable to ablation front feedthrough.[39]

A single shot was performed using a 2× graded doped ablator that was ~20 μm thicker than the ~209 μm thick standard design used in all previous shots. The capsule was driven in a uranium hohlraum using a pulse with a peak power that was increased to ~390 TW in order to achieve a similar velocity to that on the 2× doped standard thickness comparison shot (N120408) described in Sec. V C 3. The trough of this pulse was lengthened by ~1 ns in order to account for the longer transit time of the first shock through the thicker ablator. Delays were also made to the second, third, and fourth rises. These pulse adjustments were made via calculation alone as shock timing measurements had yet to be performed on the thicker ablator.

A comparison of the data from the thicker ablator shot (N120418) with that from a similar standard ablator shot (N120408) is shown in Fig. 17. Both shots had similar peak velocities, again by design. The similar mass remaining *fraction* for the two shots meant that the absolute mass remaining for the thicker shell was ~10% larger (since its initial mass was ~10% larger). Measured remaining shell thicknesses were comparable to within experimental errors, though still larger than given by simulations. Overall, the differences between the thicker and standard ablators largely followed expectations.

Higher neutron yields and ion temperatures were observed using the thicker shell, consistent with the capsule being more robust to mix penetration from the ablation front. As in Sec. V C 2, these differences in core performance were not obviously reflected in the radiographic data alone.

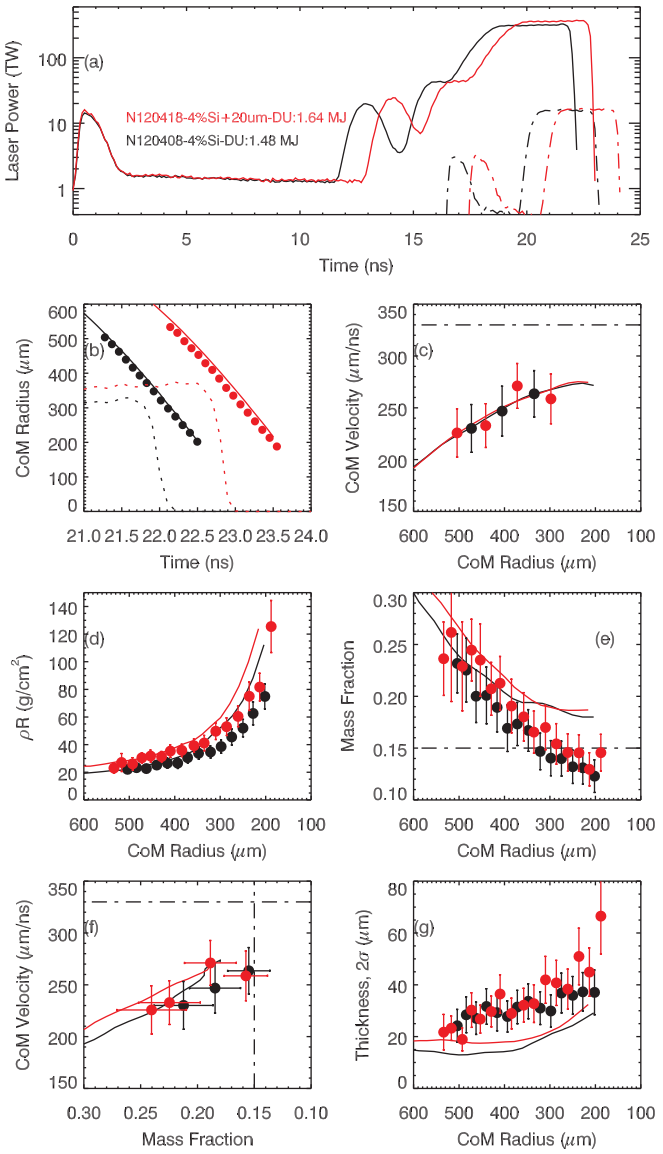

FIG. 17. Comparison of the dynamics of a thicker shell implosion (N120418) with the standard-thickness shell (N120408). Both capsules use the 2× graded doped design. The thicker shell is driven with a longer and higher power pulse designed to give a similar peak velocity. The similar fractional mass remaining between the shots means that the thicker shell has a ~10% larger absolute final mass (since its initial mass is ~10% larger).

D. Cryogenic surrogacy

All the *ConA* shots described thus far were gas-filled capsules designed with an additional inner 14 μm of pure CH to match the mass of a 69 μm solid DT fuel layer (see Sec. II D). Since the global dynamics of the implosion (radial trajectory, velocity, remaining mass) is primarily sensitive to the initial mass and outer radius of the shell, these capsules represent surrogates for a layered target at least up to peak velocity.

To test the validity of this surrogacy, a single *THDConA* shot was performed. The solid fuel layer was 74% T, 24% H, and 2% D by atomic fraction rather than equimolar DT in order to reduce the neutron yield.[46] Details of the fielding of DT and THD layered shots have been described in detail elsewhere.[23] The only difference with this target was the presence of horizontal slits in the hohlraum to provide radiography access.

Complicating the surrogacy test was the use of a gold hohlraum on the *THDConA* target. Only uranium hohlraum *ConA* targets had been shot in the campaign using the low-coast pulse shape. To generate an equivalent capsule drive history in the gold hohlraum, the *THDConA* (N120329) was shot with a pulse that had ~8% higher peak power than the

equivalent uranium hohlraum shot (N120306). A further difference was that the *THDConA* capsule had a 13 μm smaller outer radius. Ultimately, these differences could only be accounted for by comparing both shots with simulations.

Results are shown in Fig. 18, comparing the layered shot to the comparable gas-filled shot. The slightly larger *ConA* capsule resulted in a later trajectory and bang time. By design, velocities were similar. Importantly, the measured remaining mass of the *THDConA* was 5%–6% lower than that of the *ConA*, the difference corresponding to the mass (ζ) of the additional CH payload in the *ConA* target. While the overall mass of the two capsules was identical, the fuel mass in the *THDConA* target is not recorded by radiography.

Verifying this mass difference was an important check on the validity of the analysis algorithm (Sec. III). One concern was that pre-heat of, or blow-off from, the inner CH layer would make this part of the ablator invisible, resulting in an underestimate of the remaining mass. The fact that removing most of this pure CH layer in the THD target resulted in the appropriate drop in mass indicates that this inner ~6% of mass was correctly accounted for in the *ConA* target.

Shell thicknesses were similar between the two shots, with both larger than simulations. Importantly, the simulations indicated that the *ConA* target, with the larger remaining mass, was expected to have a larger shell thickness late in time, contrary to what was observed. This may indicate that some of the fuel layer is mixing with the CH, lowering the density of ablator material, and producing a thicker ablator.

The measured neutron down-scattered ratio[21] was $6.34\% \pm 0.58\%$, the highest observed on the NIF to date, corresponding to an estimated fuel ρR of $\sim 1.3\,\mathrm{g/cm^3}$. This was a significant improvement from the $4.4\% \pm 0.15\%$ reported[22] on the ~420 TW low-coast pulses, though still below the ignition requirement[73] of 7%. The significant improvement in ρR indicates that implosions driven by the shorter pulses were allowing the fuel to decompress during the coasting phase. This decompression is not captured in simulations and suggests the ablation pressure after the laser turns off is dropping more quickly than expected.

These results indicate that the standard gas-filled *ConA* target is a good surrogate for the global implosion dynamics of layered targets, at least up to peak velocity. Deviations are expected—and could potentially be observed—during the deceleration phase and final convergence. The dynamics of the rebounding shock and how the fuel assembles after peak velocity and prior to stagnation is a largely unexplored part of the implosion.

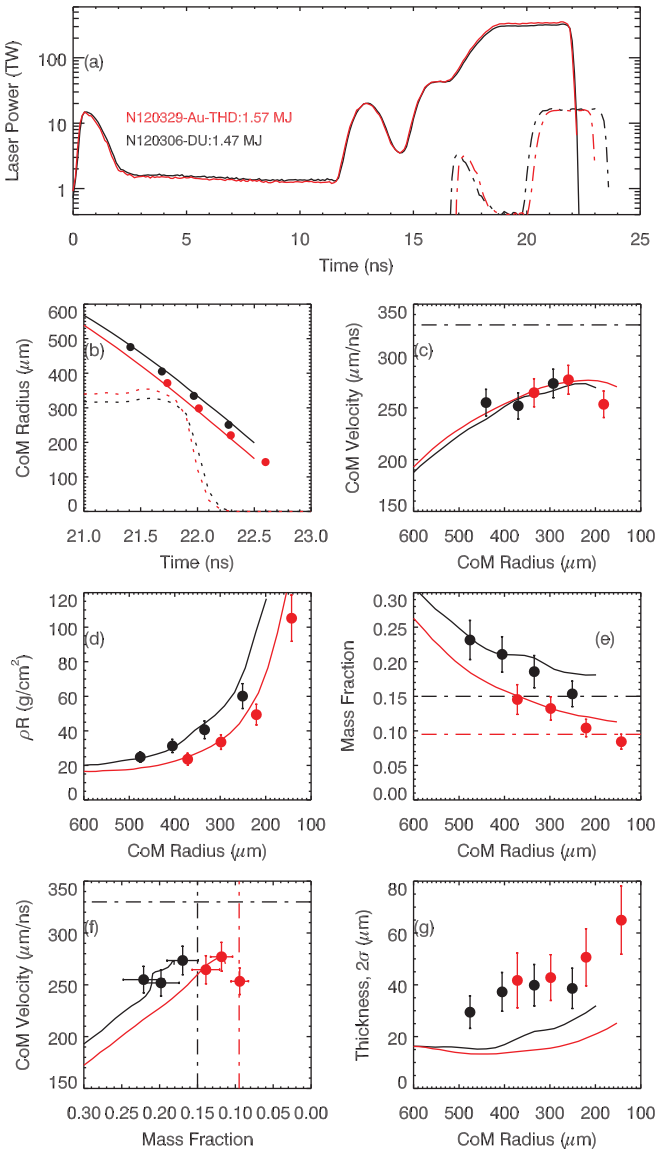

FIG. 18. Data for a layered "*THDConA*" capsule (N120329) in a gold hohlraum as compared to a standard gas-filled *ConA* capsule (N120306) in a uranium hohlraum. Similar capsule velocities were achieved by design, with the gold hohlraum being driven at ~8% higher peak power. Replacing the additional CH payload with the x-ray transparent THD layer results in a lower mass observed in the THD-ConA target as expected.

VI. DISCUSSION

General trends in the measured capsule velocity, mass, and thickness emerge, independent of laser pulse shape, ablator dopant, or hohlraum type. An assessment of these three trends is given along with a summary of results for specific experimental comparisons.

A. Low velocity at a given laser power

Implosion velocities are ~8%-12% lower than baseline simulations[70] that account for known losses and that are forced to match the shock timing measurements. The resulting capsule trajectories give the appearance of having been driven by a laser with 13%–15% less energy (~200 kJ) than delivered, a deficit that has prevented the ignition velocity requirement from being achieved in this study. Such an apparent loss of laser energy was also observed throughout the foot of the pulse,[18,70] indicating that the conversion of laser energy to ablation pressure is overestimated for a broad range of plasma conditions. Fig. 19 summarizes the maximum velocities for each shot as a function of peak laser power.

A recent study indicates that previously reported hohlraum temperatures were too high and that better accounting of the measured LEH closure results in lower inferred temperatures.[74] Agreement of the measured Dante x-ray flux with simulations of earlier experiments[23,70] may thus have

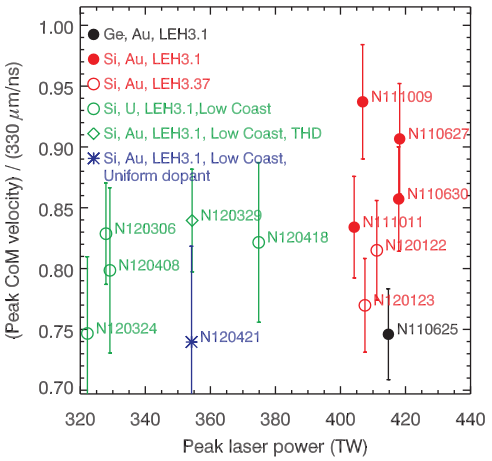

FIG. 19. Comparison of maximum measured velocity (relative to the ignition requirement) as a function of peak laser power for different shots. Low peak power shots primarily used the more efficient uranium hohlraums with the low-coast pulse, while the higher peak power shots used gold hohlraums, some with a larger LEH diameter. Shots using Ge-doped ablators, the larger LEH, or a 2% uniformly doped ablator resulted in lower velocities for a given peak laser power.

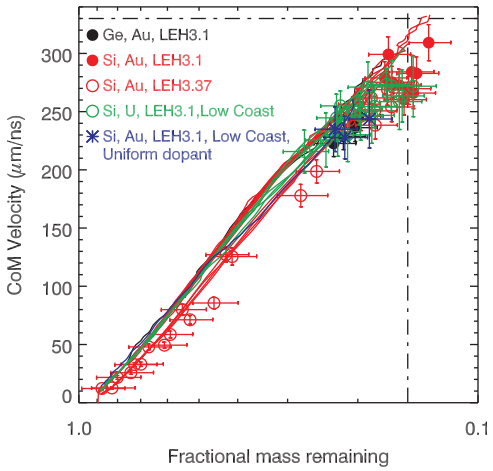

FIG. 20. The path of the rocket curve relating velocity to fractional mass remaining is expected to be weakly dependent on pulse shape and dopant, allowing data from many different experiments to be co-plotted. Here, only data taken at radii larger than 300 μm are shown to focus on the acceleration phase of the implosion. Experimental data generally have lower masses than simulations at a fixed velocity, suggesting a lower-than-expected ablation efficiency throughout the implosion. The simulated curve for Ge-doped capsules, on which the ignition requirements were set, lies at the upper limit of the envelope of curves for Si-doped capsules, indicating that the lower-Z ablator is slightly less ablatively efficient. Note that the dotted-dashed lines represent the Rev5 ignition requirements as established for Ge-doped capsules.[5]

been the result of offsetting errors: Simulations had overestimated hohlraum temperatures but underestimated the LEH diameter, resulting in a total emitted power being close to experiment. How much of the velocity discrepancy is due to the over-estimate of x-ray flux produced by the hohlraum and how much is due to inaccuracies in the radiation transport and ablative response of the capsule remains unclear.

Scaling from current results indicates that the ignition velocity requirement should be achievable for the current capsule thickness if uranium hohlraums are used. The single Au hohlraum shot that reached 93% ± 5% of the required velocity using 420 TW and 1.5 MJ indicates that with the ~4% increase in velocity expected by switching to a uranium hohlraum and the 2% increase gained by not having backlighter beams, peak velocities should be within 99% of the requirement for nominal thickness capsules driven at 420 TW.[44] As discussed next, however, the need to move towards thicker shells will make it more challenging to reach velocity requirements within current NIF facility limits.

B. Low mass at a given velocity

Shell masses are already at, or below, the minimum requirement even though ignition velocities have yet to be reached. This suggests that ablation front growth into the fuel and hotspot could already be of concern at drive conditions well below those required to achieve ignition.

The mass remaining for a given achieved velocity is referred to here as the ablation efficiency: more efficient ablators reach a given velocity with less mass ablated. A comparison of the simulated versus measured velocity and mass for the various shots is shown in Fig. 20 and indicates a less-than-expected ablation efficiency. Thus, capsules reaching only 85%–90% of the ignition velocity requirement have already reached the minimum mass requirement. Increasing the drive to raise velocities, therefore, risks generating further hydrodynamic mix.[75]

This velocity-mass curve is of fundamental importance as its path (though not its maximum) is relatively insensitive to the different laser and hohlraum conditions. This path is primarily a function of the intrinsic properties of the ablator, its EOS (which determines the sound speed) and opacity (which determines the ablation front thickness), rather than the flux incident on it, although the hardness of the drive spectrum plays a role. Since the rocket equation[3,8] relates the velocity and mass via the exhaust velocity (v_{ex}) by $dV/(d\ln M) = v_{ex}$, a low ablation efficiency indicates a low exhaust velocity over at least part of the drive history. Simulations of Ge-doped capsules, which were used to set the ignition requirements,[5] have a slightly higher rocket efficiency than those for Si-doped capsules. This means that the Si-doped simulations reach ignition velocity with less mass than the requirements, with experimental data exhibiting even lower mass.

The twin problems of a low laser-to-ablator coupling and a low ablation efficiency have thus resulted in the severe problem of an implosion with low velocity and low mass. The practical implications of this are that thicker capsules and higher laser powers are required to achieve ignition. Scaling to capsules that are 20 μm thicker than current designs indicate that laser powers at, or slightly beyond, the 500 TW facility limit are required to achieve the required velocity and mass remaining. Capsules that are 40 μm thicker would require laser powers well beyond current capabilities. These results indicate the importance of undertaking a study of other ablator materials, particularly those with potentially improved rocket efficiency such as beryllium.

C. Larger thickness at a given radius

The measured ablator thickness is larger than simulations, particularly around the time of peak velocity. This result is consistent across all shots, except for a single high-

foot (high adiabat) implosion performed at the beginning of the experimental series (see Sec. V A). Though extending the pulse reduced the thickness, the proportional difference to simulations was still comparable. The discrepancy begins at the 4th rise, where shock timing measurements end, and continues throughout the main pulse and afterwards.

On-going work indicates that some of this discrepancy may be the result of finer details in the x-ray drive history that are not captured by simply reducing the peak laser power by a constant (13%–15%) as shown above. Exactly matching the measured capsule radius versus time, instead of just approximating it as shown in this paper, results in an ablator thickness much closer to measured values. This provides a self-consistent check of the dynamics of the implosion, relating the ablation pressure to the ablator compressibility. Importantly, these results suggest that the thick shell late in time is caused by a sudden drop in drive as the ablation front enters the Si dopant.

Unlike for the measurement of low velocity and low mass, the implications of a thicker shell are less obvious. A low density ablator is indicative of a higher shell adiabat, providing less free energy to do work and leading to lower hotspot pressures. It could also result in a more hydrodynamically unstable ablator-fuel interface, although initial attempts to mitigate this using heavier dopant fractions do not appear to have produced a noticeable improvement in neutron yield or fuel ρR (see Sec. V C 2).

D. Summary of specific experimental comparisons

Many of the shots were set up to compare different experimental configurations in an effort to guide prospective design changes. Here, the results and their implications are summarized

(1) Si-doped CH results in a higher ablation pressure than Ge-doped CH when dopant concentrations are set to produce comparable pre-heat levels (Sec. V B 1). For the same laser power and capsule sizes, 2% Si-doped ablators give 5%–7% higher velocities than 1% Ge-doped ablators. This difference appears to be slightly larger than expected from simulations.
(2) Extending the pulse is an effective strategy for increasing velocity. This is in part because the lower-than-expected velocities for a given laser power mean that the laser turns off when the capsule is only at 60%–70% of its initial radius, rather than ~50%. (Sec. V B 2). Also, evidence from the capsule trajectory and thickness suggests that the drive decreases faster than expected when the laser turns off.
(3) Slower rise times on the main laser pulse appear to be more efficient at coupling laser energy to capsule kinetic energy. Although the slower (3 ns) rise was expected to have a lower velocity than the nominal (2 ns) rise, simply for geometric reasons, velocities were in fact similar. The faster (1 ns) had the lowest peak velocity, opposite to predictions, indicating a faster rises have a larger energy deficit than slower rises (Sec. V B 3).
(4) Increasing the Si dopant concentration in the graded doped design makes no measurable difference to velocity or mass but may slightly reduce thickness (Sec. V C 2). Neutron yields for the more heavily doped design were lower, indicating that the ablation front instability is worse with more dopant (as expected, given the steeper ablation front).
(5) A uniform dopant reduces velocity and increases shell thickness, resulting in a significant drop in neutron yield and temperature and suggesting[76] significant ablator-gas mix in the core (Sec. V C 2). Again, this points to an unstable ablation front, at least in the more heavily doped capsules.
(6) Surrogacy between layered capsules and gas-filled capsules appears to be adequate for the acceleration phase. The absence of the 6% CH surrogate mass payload was detected in the THD capsule (Sec. V D), providing a useful check of the systematics of the mass measurement.
(7) The highest measured neutron down-scattered fraction measured to date was obtained with the extended, low-coast laser pulse, suggesting that unexpected decompression of the fuel was occurring with a shorter main pulse. This may be related to the larger shell thickness late in time, which is also indicative of a late-time drop in the drive pressure.

As mentioned above, most of these different design configurations were tested on companion layered DT shots in order to examine integrated performance. Simulations were adjusted to match the observed radius versus time of companion *ConA* shots. This semi-empirical approach effectively ignores the simulated laser-hohlraum-capsule interaction and sets the late time boundary condition for the implosion to be the experimental capsule trajectory. While this approach does result in improved agreement with many observables, simulated neutron yields and stagnation pressures are still too high.[70]

It is worth mentioning that, while the measurements described here capture the evolution of several fundamental parameters required for ignition, they are only a probe of the temporal and spatial behavior of the capsule at scales greater than ~100 ps and ~10 μm. Ignition is also extremely sensitive to smaller-scale features of the implosion: Strong shock waves, either during acceleration or deceleration, can have a large effect on the 1-D implosion behavior while 3-D performance is heavily influenced by fine-scale features in hydrodynamic instability growth. This high-frequency information is not directly accessible late in the implosion using the current experimental platform due to temporal and spatial resolution limits. Modifications are underway to improve the resolution of detectors and imaging systems to better access these finer scale details but it is likely that the problem of unresolved, yet important, features will always exist.

VII. CONCLUSIONS

The original Ge-doped CH capsule and Au hohlraum point design has been found to reach only 75% of the ignition velocity requirement when driven by a 1.3-MJ shock-timed pulse. Switching to Si-doped CH and extending the pulse to 1.5 MJ has brought the velocity up to 93% of this requirement, with a 4% additional improvement expected by

switching to uranium hohlraums. These velocities were 8%–12% lower than baseline designs adjusted to fit shock timing data and accounting for known losses.

Even at ~90% of ignition velocity, measured ablator masses are at, or below, the minimum set by stability requirements. This suggests a lower-than-expected ablation efficiency for CH and indicates that raising the drive pressure any further, as is necessary to increase velocity, would push the capsule well into the hydrodynamically unstable regime. Both these results indicate that a thicker ablator, and laser powers potentially up to, or beyond, the 500 TW facility limit, are required in order to achieve ignition.

The inability of current simulations to model experiments at the level of accuracy necessary for ignition raises the question of whether the ignition requirements themselves are correct since these are set by aspects of the same simulations. In particular, preliminary evidence suggests that the remaining mass requirement needs to be set higher, with mix already occurring before this limit has been reached. Whether the velocity requirement is sufficient remains to be seen.

Many of the changes made throughout this study were not in the original tuning plan, a wider search necessitated by the lower-than-expected velocities and neutron yields in all implosions. This suggests that the original multi-dimensional iterative method may need to be revisited. Such an approach[13] was based on the assumption that a global optimization could be achieved by locally improving performance at each tuning step. While this type of greedy algorithm[77] was expected to converge when the initial guess was close to the goal (such that tuning steps are small, sensitivities are linear, and cross-coupling between changing inputs is negligible), a more sophisticated search algorithm, and many more shots, may be necessary to navigate the rugged landscape in which current experiments likely find themselves.

A parallel approach is to upgrade existing high energy density physics models to improve the "first guess" at the experimental inputs required for ignition. Though integrated implosion experiments have now demonstrated that uncertainties in existing models were considerably underestimated they do not convincingly identify which model is at fault, or which physics may be missing. For example, low velocities at a given laser power may be caused by several effects: a less efficient laser-to-x-ray conversion at the hohlraum wall, incorrect gold expansion velocities at the LEH, inaccurate radiation transport through an ablating plasma of many optical depths, or a poorly modeled opacity or EOS for carbon transitioning from Li-like to H-like ionization as it passes through the ablation front. A new generation of highly accurate measurements will be required to isolate and quantify each one of these elements at the level required to successfully navigate the path to ignition at the scale of $\lesssim$2 MJ.

ACKNOWLEDGMENTS

This work was performed under the auspices of the U.S. Department of Energy by Lawrence Livermore National Laboratory under Contract DE-AC52-07NA27344.

APPENDIX: AN INVERSE METHOD FOR INFERRING $\kappa_\nu(r)\rho(r)$ WHEN THE BACKLIGHTER PROFILE IS UNKNOWN

An inverse Abel approach is described, which provides a robust method for extracting the opacity-density profile ($\kappa_\nu(r)\rho(r)$) of a shell radiographed with a smooth, but unknown, backlighter profile.

For absorption contrast radiography, the observed x-ray intensity, $I(y)$, along a measured dimension, y, where $y=0$ corresponds to the center of the object with spherical symmetry, is given by

$$I(y)/I_0(y) = \exp[-\tau(y)], \tag{A1}$$

where $I_0(y)$ is the unknown initial x-ray intensity and $\tau(y)$ is the optical depth along the line of sight.

Taking the logarithm and re-arranging Eq. (A1) gives

$$\tau(y) = -\ln I(y) + \ln I_0(y). \tag{A2}$$

Typically, both $I(y)$ and $I_0(y)$ are measured or known, thus giving $\tau(y)$ and allowing $\kappa_\nu(r)\rho(r)$ to be determined explicitly from the inverse Abel transform, $A^{-1}[\tau(y)]$

$$\kappa_\nu(r)\rho(r) = A^{-1}[\tau(y)], \tag{A3}$$

$$= -\frac{1}{\pi}\int_r^\infty \frac{d\tau(y)}{dy}\frac{dy}{\sqrt{y^2-r^2}}. \tag{A4}$$

If $I_0(y)$ is not known *a priori*, the inverse Abel transform can still be performed on Eq. (A2), giving

$$\kappa_\nu(r)\rho(r) = -A^{-1}[\ln I(y)] + A^{-1}[\ln I_0(y)]. \tag{A5}$$

The combination of the logarithm and the inverse Abel transform turns the unknown $I_0(y)$ into an *additive* background, $A^{-1}[\ln I_0(y)]$, upon which the shell profile sits. Separating the shell profile from the background profile is much like separating a spectral line from its low-level background. Fitting a Gaussian to a quadratic background has been found to work accurately when analyzing each limb independently.

Determining $I_0(y)$ in the inverse space as described here is more robust than determining it in the image space described before,[19] despite the presence of increased noise cause by the inversion. This is because the inverse Abel transform (which involves a derivative) magnifies the difference between the high frequency shell feature and the low frequency backlighter profile, in effect acting like a high pass filter to smooth out the backlighter profile relative to the shell profile. The inverse approach was found to be particularly useful when analyzing radiographs of more heavily doped capsules.

[1]J. Lindl, Phys. Plasmas **2**, 3933 (1995).
[2]J. D. Lindl, P. Amendt, R. L. Berger, S. G. Glendinning, S. H. Glenzer, S. W. Haan, R. L. Kauffman, O. L. Landen, and L. J. Suter, Phys. Plasmas **11**, 339 (2004).
[3]S. Atzeni and J. MeyerterVehn, *The Physics of Inertial Fusion* (Oxford University Press, Oxford, U.K., 2007).
[4]D. S. Clark, S. W. Haan, and J. D. Salmonson, Phys. Plasmas **15**, 056305 (2008).

[5]S. W. Haan, J. D. Lindl, D. A. Callahan, D. S. Clark, J. D. Salmonson, B. A. Hammel, L. J. Atherton, R. C. Cook, M. J. Edwards, S. Glenzer, A. V. Hamza, S. P. Hatchett, M. C. Herrmann, D. E. Hinkel, D. D. Ho, H. Huang, O. S. Jones, J. Kline, G. Kyrala, O. L. Landen, B. J. MacGowan, M. M. Marinak, D. D. Meyerhofer, J. L. Milovich, K. A. Moreno, E. I. Moses, D. H. Munro, A. Nikroo, R. E. Olson, K. Peterson, S. M. Pollaine, J. E. Ralph, H. F. Robey, B. K. Spears, P. T. Springer, L. J. Suter, C. A. Thomas, R. P. Town, R. Vesey, S. V. Weber, H. L. Wilkens, and D. C. Wilson, Phys. Plasmas **18**, 051001 (2011).
[6]M. Herrmann, M. Tabak, and J. Lindl, Nucl. Fusion **41**, 99 (2001).
[7]A. Kemp, J. Meyer-ter Vehn, and S. Atzeni, Phys. Rev. Lett. **86**, 3336 (2001).
[8]Y. Saillard, Nucl. Fusion **46**, 1017 (2006).
[9]B. Hammel, S. Haan, D. Clark, M. Edwards, S. Langer, M. Marinak, M. Patel, J. Salmonson, and H. Scott, High Energy Density Phys. **6**, 171 (2010).
[10]D. S. Clark, S. W. Haan, A. W. Cook, M. J. Edwards, B. A. Hammel, J. M. Koning, and M. M. Marinak, Phys. Plasmas **18**, 082701 (2011).
[11]D. S. Clark, S. W. Haan, B. A. Hammel, J. D. Salmonson, D. A. Callahan, and R. P. J. Town, Phys. Plasmas **17**, 052703 (2010).
[12]G. H. Miller, E. I. Moses, and C. R. Wuest, Nucl. Fusion **44**, S228 (2004).
[13]O. L. Landen, J. Edwards, S. W. Haan, H. F. Robey, J. Milovich, B. K. Spears, S. V. Weber, D. S. Clark, J. D. Lindl, B. J. MacGowan, E. I. Moses, J. Atherton, P. A. Amendt, T. R. Boehly, D. K. Bradley, D. G. Braun, D. A. Callahan, P. M. Celliers, G. W. Collins, E. L. Dewald, L. Divol, J. A. Frenje, S. H. Glenzer, A. Hamza, B. A. Hammel, D. G. Hicks, N. Hoffman, N. Izumi, O. S. Jones, J. D. Kilkenny, R. K. Kirkwood, J. L. Kline, G. A. Kyrala, M. M. Marinak, N. Meezan, D. D. Meyerhofer, P. Michel, D. H. Munro, R. E. Olson, A. Nikroo, S. P. Regan, L. J. Suter, C. A. Thomas, and D. C. Wilson, Phys. Plasmas **18**, 051002 (2011).
[14]B. A. Hammel, Plasma Phys. Controlled Fusion **48**, B497 (2006).
[15]O. L. Landen, T. R. Boehly, D. K. Bradley, D. G. Braun, D. A. Callahan, P. M. Celliers, G. W. Collins, E. L. Dewald, L. Divol, S. H. Glenzer, A. Hamza, D. G. Hicks, N. Hoffman, N. Izumi, O. S. Jones, R. K. Kirkwood, G. A. Kyrala, P. Michel, J. Milovich, D. H. Munro, A. Nikroo, R. E. Olson, H. F. Robey, B. K. Spears, C. A. Thomas, S. V. Weber, D. C. Wilson, M. M. Marinak, L. J. Suter, B. A. Hammel, D. D. Meyerhofer, J. Atherton, J. Edwards, S. W. Haan, J. D. Lindl, B. J. MacGowan, and E. I. Moses, Phys. Plasmas **17**, 056301 (2010).
[16]G. A. Kyrala, J. L. Kline, S. Dixit, S. Glenzer, D. Kalantar, D. Bradley, N. Izumi, N. Meezan, O. Landen, D. Callahan, S. V. Weber, J. P. Holder, S. Glenn, M. J. Edwards, J. Koch, L. J. Suter, S. W. Haan, R. P. J. Town, P. Michel, O. Jones, S. Langer, J. D. Moody, E. L. Dewald, T. Ma, J. Ralph, A. Hamza, E. Dzenitis, and J. Kilkenny, Phys. Plasmas **18**, 056307 (2011).
[17]H. F. Robey, T. R. Boehly, P. M. Celliers, J. H. Eggert, D. Hicks, R. F. Smith, R. Collins, M. W. Bowers, K. G. Krauter, P. S. Datte, D. H. Munro, J. L. Milovich, O. S. Jones, P. A. Michel, C. A. Thomas, R. E. Olson, S. Pollaine, R. P. J. Town, S. Haan, D. Callahan, D. Clark, J. Edwards, J. L. Kline, S. Dixit, M. B. Schneider, E. L. Dewald, K. Widmann, J. D. Moody, T. Doppner, H. B. Radousky, A. Throop, D. Kalantar, P. DiNicola, A. Nikroo, J. J. Kroll, A. V. Hamza, J. B. Horner, S. D. Bhandarkar, E. Dzenitis, E. Alger, E. Giraldez, C. Castro, K. Moreno, C. Haynam, K. N. LaFortune, C. Widmayer, M. Shaw, K. Jancaitis, T. Parham, D. M. Holunga, C. F. Walters, B. Haid, E. R. Mapoles, J. Sater, C. R. Gibson, T. Malsbury, J. Fair, D. Trummer, K. R. Coffee, B. Burr, L. V. Berzins, C. Choate, S. J. Brereton, S. Azevedo, H. Chandrasekaran, D. C. Eder, N. D. Masters, A. C. Fisher, P. A. Sterne, B. K. Young, O. L. Landen, B. M. V. Wonterghem, B. J. MacGowan, J. Atherton, J. D. Lindl, D. D. Meyerhofer, and E. Moses, Phys. Plasmas **19**, 042706 (2012).
[18]H. F. Robey, P. M. Celliers, J. L. Kline, A. J. Mackinnon, T. R. Boehly, O. L. Landen, J. H. Eggert, D. Hicks, S. Le Pape, D. R. Farley, M. W. Bowers, K. G. Krauter, D. H. Munro, O. S. Jones, J. L. Milovich, D. Clark, B. K. Spears, R. P. J. Town, S. W. Haan, S. Dixit, M. B. Schneider, E. L. Dewald, K. Widmann, J. D. Moody, T. D. Döppner, H. B. Radousky, A. Nikroo, J. J. Kroll, A. V. Hamza, J. B. Horner, S. D. Bhandarkar, E. Dzenitis, E. Alger, E. Giraldez, C. Castro, K. Moreno, C. Haynam, K. N. LaFortune, C. Widmayer, M. Shaw, K. Jancaitis, T. Parham, D. M. Holunga, C. F. Walters, B. Haid, T. Malsbury, D. Trummer, K. R. Coffee, B. Burr, L. V. Berzins, C. Choate, S. J. Brereton, S. Azevedo, H. Chandrasekaran, S. Glenzer, J. A. Caggiano, J. P. Knauer, J. A. Frenje, D. T. Casey, M. Gatu Johnson, F. H. Séguin, B. K. Young, M. J. Edwards, B. M. Van Wonterghem, J. Kilkenny, B. J. MacGowan, J. Atherton, J. D. Lindl, D. D. Meyerhofer, and E. Moses, Phys. Rev. Lett. **108**, 215004 (2012).
[19]D. G. Hicks, B. K. Spears, D. G. Braun, R. E. Olson, C. M. Sorce, P. M. Celliers, G. W. Collins, and O. L. Landen, Phys. Plasmas **17**, 102703 (2010).
[20]J. A. Frenje, D. T. Casey, C. K. Li, F. H. Seguin, R. D. Petrasso, V. Y. Glebov, P. B. Radha, T. C. Sangster, D. D. Meyerhofer, S. P. Hatchett, S. W. Haan, C. J. Cerjan, O. L. Landen, K. A. Fletcher, and R. J. Leeper, Phys. Plasmas **17**, 056311 (2010).
[21]M. G. Johnson, J. A. Frenje, D. T. Casey, C. K. Li, F. H. Séguin, R. Petrasso, R. Ashabranner, R. M. Bionta, D. L. Bleuel, E. J. Bond, J. A. Caggiano, A. Carpenter, C. J. Cerjan, T. J. Clancy, T. Doeppner, M. J. Eckart, M. J. Edwards, S. Friedrich, S. H. Glenzer, S. W. Haan, E. P. Hartouni, R. Hatarik, S. P. Hatchett, O. S. Jones, G. Kyrala, S. L. Pape, R. A. Lerche, O. L. Landen, T. Ma, A. J. MacKinnon, M. A. McKernan, M. J. Moran, E. Moses, D. H. Munro, J. McNaney, H. S. Park, J. Ralph, B. Remington, J. R. Rygg, S. M. Sepke, V. Smalyuk, B. Spears, P. T. Springer, C. B. Yeamans, M. Farrell, D. Jasion, J. D. Kilkenny, A. Nikroo, R. Paguio, J. P. Knauer, V. Y. Glebov, T. C. Sangster, R. Betti, C. Stoeckl, J. Magoon, M. J. Shoup III, G. P. Grim, J. Kline, G. L. Morgan, T. J. Murphy, R. J. Leeper, C. L. Ruiz, G. W. Cooper, and A. J. Nelson, Rev. Sci. Instrum. **83**, 10D308 (2012).
[22]A. J. Mackinnon, J. L. Kline, S. N. Dixit, S. H. Glenzer, M. J. Edwards, D. A. Callahan, N. B. Meezan, S. W. Haan, J. D. Kilkenny, T. Döppner, D. R. Farley, J. D. Moody, J. E. Ralph, B. J. MacGowan, O. L. Landen, H. F. Robey, T. R. Boehly, P. M. Celliers, J. H. Eggert, K. Krauter, G. Frieders, G. F. Ross, D. G. Hicks, R. E. Olson, S. V. Weber, B. K. Spears, J. D. Salmonsen, P. Michel, L. Divol, B. Hammel, C. A. Thomas, D. S. Clark, O. S. Jones, P. T. Springer, C. J. Cerjan, G. W. Collins, V. Y. Glebov, J. P. Knauer, C. Sangster, C. Stoeckl, P. McKenty, J. M. McNaney, R. J. Leeper, C. L. Ruiz, G. W. Cooper, A. G. Nelson, G. G. A. Chandler, K. D. Hahn, M. J. Moran, M. B. Schneider, N. E. Palmer, R. M. Bionta, E. P. Hartouni, S. LePape, P. K. Patel, N. Izumi, R. Tommasini, E. J. Bond, J. A. Caggiano, R. Hatarik, G. P. Grim, F. E. Merrill, D. N. Fittinghoff, N. Guler, O. Drury, D. C. Wilson, H. W. Herrmann, W. Stoeffl, D. T. Casey, M. G. Johnson, J. A. Frenje, R. D. Petrasso, A. Zylestra, H. Rinderknecht, D. H. Kalantar, J. M. Dzenitis, P. Di Nicola, D. C. Eder, W. H. Courdin, G. Gururangan, S. C. Burkhart, S. Friedrich, D. L. Blueuel, l. A. Bernstein, M. J. Eckart, D. H. Munro, S. P. Hatchett, A. G. Macphee, D. H. Edgell, D. K. Bradley, P. M. Bell, S. M. Glenn, N. Simanovskaia, M. A. Barrios, R. Benedetti, G. A. Kyrala, R. P. J. Town, E. L. Dewald, J. L. Milovich, K. Widmann, A. S. Moore, G. LaCaille, S. P. Regan, L. J. Suter, B. Felker, R. C. Ashabranner, M. C. Jackson, R. Prasad, M. J. Richardson, T. R. Kohut, P. S. Datte, G. W. Krauter, J. J. Klingman, R. F. Burr, T. A. Land, M. R. Hermann, D. A. Latray, R. L. Saunders, S. Weaver, S. J. Cohen, L. Berzins, S. G. Brass, E. S. Palma, R. R. Lowe-Webb, G. N. McHalle, P. A. Arnold, L. J. Lagin, C. D. Marshall, G. K. Brunton, D. G. Mathisen, R. D. Wood, J. R. Cox, R. B. Ehrlich, K. M. Knittel, M. W. Bowers, R. A. Zacharias, B. K. Young, J. P. Holder, J. R. Kimbrough, T. Ma, K. N. La Fortune, C. C. Widmayer, M. J. Shaw, G. V. Erbert, K. S. Jancaitis, J. M. DiNicola, C. Orth, G. Heestand, R. Kirkwood, C. Haynam, P. J. Wegner, P. K. Whitman, A. Hamza, E. G. Dzenitis, R. J. Wallace, S. D. Bhandarkar, T. G. Parham, R. Dylla-Spears, E. R. Mapoles, B. J. Kozioziemski, J. D. Sater, C. F. Walters, B. J. Haid, J. Fair, A. Nikroo, E. Giraldez, K. Moreno, B. Vanwonterghem, R. L. Kauffman, S. Batha, D. W. Larson, R. J. Fortner, D. H. Schneider, J. D. Lindl, R. W. Patterson, L. J. Atherton, and E. I. Moses, Phys. Rev. Lett. **108**, 215005 (2012).
[23]S. H. Glenzer, D. A. Callahan, A. J. MacKinnon, J. L. Kline, G. Grim, E. T. Alger, R. L. Berger, L. A. Bernstein, R. Betti, D. L. Bleuel, T. R. Boehly, D. K. Bradley, S. C. Burkhart, R. Burr, J. A. Caggiano, C. Castro, D. T. Casey, C. Choate, D. S. Clark, P. Celliers, C. J. Cerjan, G. W. Collins, E. L. Dewald, P. DiNicola, J. M. DiNicola, L. Divol, S. Dixit, T. Doppner, R. Dylla-Spears, E. Dzenitis, M. Eckart, G. Erbert, D. Farley, J. Fair, D. Fittinghoff, M. Frank, L. J. A. Frenje, S. Friedrich, D. T. Casey, M. G. Johnson, C. Gibson, E. Giraldez, V. Glebov, S. Glenn, N. Guler, S. W. Haan, B. J. Haid, B. A. Hammel, A. V. Hamza, C. A. Haynam, G. M. Heestand, M. Hermann, H. W. Hermann, D. G. Hicks, D. E. Hinkel, J. P. Holder, D. M. Holunda, J. B. Horner, W. W. Hsing, H. Huang, N. Izumi, M. Jackson, O. S. Jones, D. H. Kalantar, R. Kauffman, J. D. Kilkenny, R. K. Kirkwood, J. Klingmann, T. Kohut, J. P. Knauer, J. A. Koch, B. Kozioziemki, G. A. Kyrala, A. L. Kritcher, J. Kroll, K. L. Fortune, L. Lagin, O. L. Landen, D. W. Larson, D. LaTray, R. J. Leeper, S. L. Pape, J. D. Lindl, R. Lowe-Webb, T. Ma, J. McNaney, A. G. MacPhee, T. N. Malsbury, E. Mapoles, C. D. Marshall, N. B. Meezan, F. Merrill, P. Michel, J. D. Moody, A. S. Moore, M. Moran, K. A. Moreno, D. H. Munro, B. R. Nathan, A. Nikroo, R. E. Olson, C. D. Orth, A. E. Pak, P. K. Patel, T.

Parham, R. Petrasso, J. E. Ralph, H. Rinderknecht, S. P. Regan, H. F. Robey, J. S. Ross, M. D. Rosen, R. Sacks, J. D. Salmonson, R. Saunders, J. Sater, C. Sangster, M. B. Schneider, F. H. Seguin, M. J. Shaw, B. K. Spears, P. T. Springer, W. Stoeffl, L. J. Suter, C. A. Thomas, R. Tommasini, R. P. J. Town, C. Walters, S. Weaver, S. V. Weber, P. J. Wegner, P. K. Whitman, K. Widmann, C. C. Widmayer, C. H. Wilde, D. C. Wilson, B. V. Wonterghem, B. J. MacGowan, L. J. Atherton, M. J. Edwards, and E. I. Moses, Phys. Plasmas **19**, 056318 (2012).

[24]B. A. Hammel, H. A. Scott, S. P. Regan, C. Cerjan, D. S. Clark, M. J. Edwards, R. Epstein, S. H. Glenzer, S. W. Haan, N. Izumi, J. A. Koch, G. A. Kyrala, O. L. Landen, S. H. Langer, K. Peterson, V. A. Smalyuk, L. J. Suter, and D. C. Wilson, Phys. Plasmas **18**, 056310 (2011).

[25]S. P. Regan, R. Epstein, B. A. Hammel, L. J. Suter, J. Ralph, H. Scott, M. A. Barrios, D. K. Bradley, D. A. Callahan, C. Cerjan, G. W. Collins, S. N. Dixit, T. Doeppner, M. J. Edwards, D. R. Farley, S. Glenn, S. H. Glenzer, I. E. Golovkin, S. W. Haan, A. Hamza, D. G. Hicks, N. Izumi, J. D. Kilkenny, J. L. Kline, G. A. Kyrala, O. L. Landen, T. Ma, J. J. MacFarlane, R. C. Mancini, R. L. McCrory, N. B. Meezan, D. D. Meyerhofer, A. Nikroo, K. J. Peterson, T. C. Sangster, P. Springer, and R. P. J. Town, Phys. Plasmas **19**, 056307 (2012).

[26]T. R. Boehly, D. L. Brown, R. S. Craxton, R. L. Keck, J. P. Knauer, J. H. Kelly, T. J. Kessler, S. A. Kumpan, S. J. Loucks, S. A. Letzring, F. J. Marshall, R. L. McCrory, S. F. B. Morse, W. Seka, J. M. Soures, and C. P. Verdon, Opt. Commun. **133**, 495 (1997).

[27]J. T. Hunt and D. R. Spect, Opt. Eng. **28**, 461 (1989).

[28]A. Bar-Shalom, J. Oreg, W. H. Goldstein, D. Shvarts, and A. Zigler, Phys. Rev. A **40**, 3183 (1989).

[29]C. A. Iglesias and F. J. Rogers, Astrophys. J. **464**, 943 (1996).

[30]C. A. Iglesias, M. H. Chen, V. Sonnad, and B. G. Wilson, J. Quantum Spect. Rad. Trans. **81**, 227 (2003).

[31]M. A. Barrios, T. R. Boehly, D. G. Hicks, D. E. Fratanduono, J. H. Eggert, G. W. Collins, and D. D. Meyerhofer, J. Appl. Phys. **111**, 093515 (2012).

[32]S. Hamel, L. X. Benedict, P. M. Celliers, M. A. Barrios, T. R. Boehly, G. W. Collins, T. Döppner, J. H. Eggert, D. R. Farley, D. G. Hicks, J. L. Kline, A. Lazicki, S. LePape, A. J. Mackinnon, J. D. Moody, H. F. Robey, E. Schwegler, and P. A. Sterne, Phys. Rev. B **86**, 094113 (2012).

[33]R. E. Olson, R. J. Leeper, A. Nobile, J. A. Oertel, G. A. Chandler, K. Cochrane, S. C. Dropinski, S. Evans, S. W. Haan, J. L. Kaae, J. P. Knauer, K. Lash, L. P. Mix, A. Nikroo, G. A. Rochau, G. Rivera, C. Russell, D. Schroen, R. J. Sebring, D. L. Tanner, R. E. Turner, and R. J. Wallace, Phys. Plasmas **11**, 2778 (2004).

[34]R. E. Olson, G. A. Rochau, O. L. Landen, and R. J. Leeper, Phys. Plasmas **18**, 032706 (2011).

[35]N. B. Meezan, L. J. Atherton, D. A. Callahan, E. L. Dewald, S. Dixit, E. G. Dzenitis, M. J. Edwards, C. A. Haynam, D. E. Hinkel, O. S. Jones, O. Landen, R. A. London, P. A. Michel, J. D. Moody, J. L. Milovich, M. B. Schneider, C. A. Thomas, R. P. J. Town, A. L. Warrick, S. V. Weber, K. Widmann, S. H. Glenzer, L. J. Suter, B. J. MacGowan, J. L. Kline, G. A. Kyrala, and A. Nikroo, Phys. Plasmas **17**, 056304 (2010).

[36]N. B. Meezan, L. J. Atherton, E. J. Bond, D. A. Callahan, E. L. Dewald, S. Dixit, E. G. Dzenitis, M. J. Edwards, C. A. Haynam, D. E. Hinkel, O. S. Jones, O. Landen, R. A. London, P. A. Michel, J. D. Moody, J. L. Milovich, M. B. Schneider, C. A. Thomas, R. P. J. Town, A. L. Warrick, S. V. Weber, K. Widmann, S. H. Glenzer, L. J. Suter, B. J. MacGowan, J. L. Kline, G. A. Kyrala, and A. Nikroo, Phys. Plasmas **17**, 109901 (2010).

[37]S. H. Glenzer, B. J. MacGowan, P. Michel, N. B. Meezan, L. J. Suter, S. N. Dixit, J. L. Kline, G. A. Kyrala, D. K. Bradley, D. A. Callahan, E. L. Dewald, L. Divol, E. Dzenitis, M. J. Edwards, A. V. Hamza, C. A. Haynam, D. E. Hinkel, D. H. Kalantar, J. D. Kilkenny, O. L. Landen, J. D. Lindl, S. LePape, J. D. Moody, A. Nikroo, T. Parham, M. B. Schneider, R. P. J. Town, P. Wegner, K. Widmann, P. Whitman, B. K. F. Young, B. Van Wonterghem, L. J. Atherton, and E. I. Moses, Science **327**, 1228 (2010).

[38]R. P. J. Town, M. D. Rosen, P. A. Michel, L. Divol, J. D. Moody, G. A. Kyrala, M. B. Schneider, J. L. Kline, C. A. Thomas, J. L. Milovich, D. A. Callahan, N. B. Meezan, D. E. Hinkel, E. A. Williams, R. L. Berger, M. J. Edwards, L. J. Suter, S. W. Haan, J. D. Lindl, E. L. Dewald, S. Dixit, S. H. Glenzer, O. L. Landen, E. I. Moses, H. A. Scott, J. A. Harte, and G. B. Zimmerman, Phys. Plasmas **18**, 056302 (2011).

[39]B. Spears, D. Hicks, C. Velsko, M. Stoyer, H. Robey, D. Munro, S. Haan, O. Landen, A. Nikroo, and H. Huang, J. Phys.: Conf. Ser. **112**, 022003 (2008).

[40]P. Michel, S. H. Glenzer, L. Divol, D. K. Bradley, D. Callahan, S. Dixit, S. Glenn, D. Hinkel, R. K. Kirkwood, J. L. Kline, W. L. Kruer, G. A. Kyrala, S. L. Pape, N. B. Meezan, R. Town, K. Widmann, E. A. Williams, B. J. MacGowan, J. Lindl, and L. J. Suter, Phys. Plasmas **17**, 056305 (2010).

[41]P. Michel, L. Divol, R. P. J. Town, M. D. Rosen, D. A. Callahan, N. B. Meezan, M. B. Schneider, G. A. Kyrala, J. D. Moody, E. L. Dewald, K. Widmann, E. Bond, J. L. Kline, C. A. Thomas, S. Dixit, E. A. Williams, D. E. Hinkel, R. L. Berger, O. L. Landen, M. J. Edwards, B. J. MacGowan, J. D. Lindl, C. Haynam, L. J. Suter, S. H. Glenzer, and E. Moses, Phys. Rev. E **83**, 046409 (2011).

[42]C. A. Haynam, P. J. Wegner, J. M. Auerbach, M. W. Bowers, S. N. Dixit, G. V. Erbert, G. M. Heestand, M. A. Henesian, M. R. Hermann, K. S. Jancaitis, K. R. Manes, C. D. Marshall, N. C. Mehta, J. Menapace, E. Moses, J. R. Murray, M. C. Nostrand, C. D. Orth, R. Patterson, R. A. Sacks, M. J. Shaw, M. Spaeth, S. B. Sutton, W. H. Williams, C. C. Widmayer, R. K. White, S. T. Yang, and B. M. V. Wonterghem, Appl. Opt. **46**, 3276 (2007).

[43]F. Girard, J. P. Jadaud, M. Naudy, B. Villette, D. Babonneau, M. Primout, M. C. Miller, R. L. Kauffman, L. J. Suter, J. Grun, and J. Davis, Phys. Plasmas **12**, 092705 (2005).

[44]D. A. Callahan, N. B. Meezan, S. H. Glenzer, A. J. MacKinnon, L. R. Benedetti, D. K. Bradley, J. R. Celeste, P. M. Celliers, S. N. Dixit, T. Doppner, E. G. Dzentitis, S. Glenn, S. W. Haan, C. A. Haynam, D. G. Hicks, D. E. Hinkel, O. S. Jones, O. L. Landen, R. A. London, A. G. MacPhee, P. A. Michel, J. D. Moody, J. E. Ralph, H. F. Robey, M. D. Rosen, M. B. Schneider, D. J. Strozzi, L. J. Suter, R. P. J. Town, K. Widmann, E. A. Williams, M. J. Edwards, B. J. MacGowan, J. D. Lindl, L. J. Atherton, G. A. Kyrala, J. L. Kline, R. E. Olson, D. Edgell, S. P. Regan, A. Nikroo, H. Wilkins, J. D. Kilkenny, and A. S. Moore, Phys. Plasmas **19**, 056305 (2012).

[45]S. W. Haan, M. C. Herrmann, T. R. Dittrich, A. J. Fetterman, M. M. Marinak, D. H. Munro, S. M. Pollaine, J. D. Salmonson, G. L. Strobel, and L. J. Suter, Phys. Plasmas **12**, 056316 (2005).

[46]M. J. Edwards, J. D. Lindl, B. K. Spears, S. V. Weber, L. J. Atherton, D. L. Bleuel, D. K. Bradley, D. A. Callahan, C. J. Cerjan, D. Clark, G. W. Collins, J. E. Fair, R. J. Fortner, S. H. Glenzer, S. W. Haan, B. A. Hammel, A. V. Hamza, S. P. Hatchett, N. Izumi, B. Jacoby, O. S. Jones, J. A. Koch, B. J. Kozioziemski, O. L. Landen, R. Lerche, B. J. MacGowan, A. J. MacKinnon, E. R. Mapoles, M. M. Marinak, M. Moran, E. I. Moses, D. H. Munro, D. H. Schneider, S. M. Sepke, D. A. Shaughnessy, P. T. Springer, R. Tommasini, L. Bernstein, W. Stoeffl, R. Betti, T. R. Boehly, T. C. Sangster, V. Y. Glebov, P. W. McKenty, S. P. Regan, D. H. Edgell, J. P. Knauer, C. Stoeckl, D. R. Harding, S. Batha, G. Grim, H. W. Herrmann, G. Kyrala, M. Wilke, D. C. Wilson, J. Frenje, R. Petrasso, K. Moreno, H. Huang, K. C. Chen, E. Giraldez, J. D. Kilkenny, M. Mauldin, N. Hein, M. Hoppe, A. Nikroo, and R. J. Leeper, Phys. Plasmas **18**, 051003 (2011).

[47]A. B. Zylstra, J. A. Frenje, F. H. Seguin, M. J. Rosenberg, H. G. Rinderknecht, M. G. Johnson, D. T. Casey, N. Sinenian, M. J.-E. Manuel, C. J. Waugh, H. W. Sio, C. K. Li, R. D. Petrasso, S. Friedrich, K. Knittel, R. Bionta, M. McKernan, D. Callahan, G. W. Collins, E. Dewald, T. Doppner, M. J. Edwards, S. Glenzer, D. G. Hicks, O. L. Landen, R. London, A. Mackinnon, N. Meezan, R. R. Prasad, J. Ralph, M. Richardson, J. R. Rygg, S. Sepke, S. Weber, R. Zacharias, E. Moses, J. Kilkenny, A. Nikroo, T. C. Sangster, V. Glebov, C. Stoeckl, R. Olson, R. J. Leeper, J. Kline, G. Kyrala, and D. Wilson, Rev. Sci. Instrum. **83**, 10D901 (2012).

[48]W. J. Hibbard, M. D. Landon, M. D. Vergino, F. D. Lee, and J. A. Chael, Rev. Sci. Instrum. **72**, 530 (2001).

[49]J. A. Oertel, R. Aragonez, T. Archuleta, C. Barnes, L. Casper, V. Fatherley, T. Heinrichs, R. King, D. Landers, F. Lopez, P. Sanchez, G. Sandoval, L. Schrank, P. Walsh, P. Bell, M. Brown, R. Costa, J. Holder, S. Montelongo, and N. Pederson, Rev. Sci. Instrum. **77**, 10E308 (2006).

[50]J. R. Kimbrough, P. M. Bell, D. K. Bradley, J. P. Holder, D. K. Kalantar, A. G. MacPhee, and S. Telford, Rev. Sci. Instrum. **81**, 10E530 (2010).

[51]Kentech Instruments Ltd., Isis Building, Howbery Park, Wallingford, Oxfordshire, OX10 8BA, U.K.

[52]Y. P. Opachich, N. Palmer, D. Homoelle, B. Hatch, P. Bell, D. Bradley, D. Kalantar, D. Browning, J. Zuegel, and O. Landen, Rev. Sci. Instrum. **83**, 10E123 (2012).

[53]A. G. MacPhee, D. H. Edgell, E. J. Bond, D. K. Bradley, C. G. Brown, S. R. Burns, J. R. Celeste, C. J. Cerjan, M. J. Eckart, V. Y. Glebov, S. H. Glenzer, D. S. Hey, O. S. Jones, J. D. Kilkenny, J. R. Kimbrough, O. L. Landen, A. J. Mackinnon, N. B. Meezan, J. M. Parker, and R. M. Sweeney, J. Instrum. **6**, P02009 (2011).

[54]D. H. Edgell, D. K. Bradley, E. J. Bond, S. Burns, D. A. Callahan, J. Celeste, M. J. Eckart, V. Y. Glebov, D. S. Hey, G. Lacaille, J. D. Kilkenny, J. Kimbrough, A. J. Mackinnon, J. Magoon, J. Parker, T. C. Sangster, M. J. Shoup III, C. Stoeckl, T. Thomas, and A. MacPhee, Rev. Sci. Instrum. **83**, 10E119 (2012).

[55]S. M. Glenn, L. R. Benedetti, D. K. Bradley, B. A. Hammel, N. Izumi, S. F. Khan, G. A. Kyrala, T. Ma, J. L. Milovich, A. E. Pak, V. A. Smalyuk, R. Tommasini, and R. P. Town, Rev. Sci. Instrum. **83**, 10E519 (2012).
[56]V. Y. Glebov, T. C. Sangster, C. Stoeckl, J. P. Knauer, W. Theobald, K. L. Marshall, M. J. Shoup III, T. Buczek, M. Cruz, T. Duffy, M. Romanofsky, M. Fox, A. Pruyne, M. J. Moran, R. A. Lerche, J. McNaney, J. D. Kilkenny, M. J. Eckart, D. Schneider, D. Munro, W. Stoeffl, R. Zacharias, J. J. Haslam, T. Clancy, M. Yeoman, D. Warwas, C. J. Horsfield, J.-L. Bourgade, O. Landoas, L. Disdier, G. A. Chandler, and R. J. Leeper, Rev. Sci. Instrum. **81**, 10D325 (2010).
[57]E. L. Dewald, K. M. Campbell, R. E. Turner, J. P. Holder, O. L. Landen, S. H. Glenzer, R. L. Kauffman, L. J. Suter, M. Landon, M. Rhodes, and D. Lee, Rev. Sci. Instrum. **75**, 3759 (2004).
[58]J. L. Kline, K. Widmann, A. Warrick, R. E. Olson, C. A. Thomas, A. S. Moore, L. J. Suter, O. Landen, D. Callahan, S. Azevedo, J. Liebman, S. H. Glenzer, A. Conder, S. N. Dixit, P. Torres III, V. Tran, E. L. Dewald, J. Kamperschroer, L. J. Atherton, J. R. Beeler, L. Berzins, J. Celeste, C. Haynam, W. Hsing, D. Larson, B. J. MacGowan, D. Hinkel, D. Kalantar, R. Kauffman, J. Kilkenny, N. Meezan, M. D. Rosen, M. Schneider, E. A. Williams, S. Vernon, R. J. Wallace, B. V. Wonterghem, and B. K. Young, Rev. Sci. Instrum. **81**, 10E321 (2010).
[59]M. B. Schneider, O. S. Jones, N. B. Meezan, J. L. Milovich, R. P. Town, S. S. Alvarez, R. G. Beeler, D. K. Bradley, J. R. Celeste, S. N. Dixit, M. J. Edwards, M. J. Haugh, D. H. Kalantar, J. L. Kline, G. A. Kyrala, O. L. Landen, B. J. MacGowan, P. Michel, J. D. Moody, S. K. Oberhelman, K. W. Piston, M. J. Pivovaroff, L. J. Suter, A. T. Teruya, C. A. Thomas, S. P. Vernon, A. L. Warrick, K. Widmann, R. D. Wood, and B. K. Young, Rev. Sci. Instrum. **81**, 10E538 (2010).
[60]M. B. Schneider, N. B. Meezan, S. S. Alvarez, J. Alameda, S. Baker, P. M. Bell, D. K. Bradley, D. A. Callahan, J. R. Celeste, E. L. Dewald, S. N. Dixit, T. Döppner, D. C. Eder, M. J. Edwards, M. Fernandez-Perea, E. Gullikson, M. J. Haugh, S. Hau-Riege, W. Hsing, N. Izumi, O. S. Jones, D. H. Kalantar, J. D. Kilkenny, J. L. Kline, G. A. Kyrala, O. L. Landen, R. A. London, B. J. MacGowan, A. J. MacKinnon, T. J. Mccarville, J. L. Milovich, P. Mirkarimi, J. D. Moody, A. S. Moore, M. D. Myers, E. A. Palma, N. Palmer, M. J. Pivovaroff, J. E. Ralph, J. Robinson, R. Soufli, L. J. Suter, A. T. Teruya, C. A. Thomas, R. P. Town, S. P. Vernon, K. Widmann, and B. K. Young, Rev. Sci. Instrum. **83**, 10E525 (2012).
[61]E. L. Dewald, C. Thomas, S. Hunter, L. Divol, N. Meezan, S. H. Glenzer, L. J. Suter, E. Bond, J. L. Kline, J. Celeste, D. Bradley, P. Bell, R. L. Kauffman, J. Kilkenny, and O. L. Landen, Rev. Sci. Instrum. **81**, 10D938 (2010).
[62]J. D. Moody, P. Datte, K. Krauter, E. Bond, P. A. Michel, S. H. Glenzer, L. Divol, C. Niemann, L. Suter, N. Meezan, B. J. MacGowan, R. Hibbard, R. London, J. Kilkenny, R. Wallace, J. L. Kline, K. Knittel, G. Frieders, B. Golick, G. Ross, K. Widmann, J. Jackson, S. Vernon, and T. Clancy, Rev. Sci. Instrum. **81**, 10D921 (2010).
[63]J. M. Hollis, J. E. Dorband, and F. Yusef-Zadeh, Astrophys. J. **386**, 293 (1992).
[64]Y. Alhassid, N. Agmon, and R. Levine, Chem. Phys. Lett. **53**, 22 (1978).
[65]M. M. Marinak, G. D. Kerbel, N. A. Gentile, O. Jones, D. Munro, S. Pollaine, T. R. Dittrich, and S. W. Haan, Phys. Plasmas **8**, 2275 (2001).
[66]M. Rosen, H. Scott, D. Hinkel, E. Williams, D. Callahan, R. Town, L. Divol, P. Michel, W. Kruer, L. Suter, R. London, J. Harte, and G. Zimmerman, High Energy Density Phys. **7**, 180 (2011).
[67]VISTA is a relativistic LTE opacity code developed by M. H. Chen based on STA theory (Ref. 28) using Dirac-Hartree-Slater methods with Breit and QED corrections for the atomic data.
[68]R. M. More, K. H. Warren, D. A. Young, and G. B. Zimmerman, Phys. Fluids **31**, 3059 (1988).
[69]S. H. Glenzer, B. J. MacGowan, N. B. Meezan, P. A. Adams, J. B. Alfonso, E. T. Alger, Z. Alherz, L. F. Alvarez, S. S. Alvarez, P. V. Amick, K. S. Anderson, S. D. Andrews, G. J. Antonini, P. A. Arnold, D. P. Atkinson, L. Auyang, S. G. Azevedo, B. N. M. Balaoing, J. A. Baltz, F. Barbosa, G. W. Bardsley, D. A. Barker, A. I. Barnes, A. Baron, R. G. Beeler, B. V. Beeman, L. R. Belk, J. C. Bell, P. M. Bell, R. L. Berger, M. A. Bergonia, L. J. Bernardez, L. V. Berzins, R. C. Bettenhausen, L. Bezerides, S. D. Bhandarkar, C. L. Bishop, E. J. Bond, D. R. Bopp, J. A. Borgman, J. R. Bower, G. A. Bowers, M. W. Bowers, D. T. Boyle, D. K. Bradley, J. L. Bragg, J. Braucht, D. L. Brinkerhoff, D. F. Browning, G. K. Brunton, S. C. Burkhart, S. R. Burns, K. E. Burns, B. Burr, L. M. Burrows, R. K. Butlin, N. J. Cahayag, D. A. Callahan, P. S. Cardinale, R. W. Carey, J. W. Carlson, A. D. Casey, C. Castro, J. R. Celeste, A. Y. Chakicherla, F. W. Chambers, C. Chan, H. Chandrasekaran, C. Chang, R. F. Chapman, K. Charron, Y. Chen, M. J. Christensen, A. J. Churby, T. J. Clancy, B. D. Cline, L. C. Clowdus, D. G. Cocherell, F. E. Coffield, S. J. Cohen, R. L. Costa, J. R. Cox, G. M. Curnow, M. J. Dailey, P. M. Danforth, R. Darbee, P. S. Datte, J. A. Davis, G. A. Deis, R. D. Demaret, E. L. Dewald, P. Di Nicola, J. M. Di Nicola, L. Divol, S. Dixit, D. B. Dobson, T. Doppner, J. D. Driscoll, J. Dugorepec, J. J. Duncan, P. C. Dupuy, E. G. Dzenitis, M. J. Eckart, S. L. Edson, G. J. Edwards, M. J. Edwards, O. D. Edwards, P. W. Edwards, J. C. Ellefson, C. H. Ellerbee, G. V. Erbert, C. M. Estes, W. J. Fabyan, R. N. Fallejo, M. Fedorov, B. Felker, J. T. Fink, M. D. Finney, L. F. Finnie, M. J. Fischer, J. M. Fisher, B. T. Fishler, J. W. Florio, A. Forsman, C. B. Foxworthy, R. M. Franks, T. Frazier, G. Frieder, T. Fung, G. N. Gawinski, C. R. Gibson, E. Giraldez, S. M. Glenn, B. P. Golick, H. Gonzales, S. A. Gonzales, M. J. Gonzalez, K. L. Griffin, J. Grippen, S. M. Gross, P. H. Gschweng, G. Gururangan, K. Gu, S. W. Haan, S. R. Hahn, B. J. Haid, J. E. Hamblen, B. A. Hammel, A. V. Hamza, D. L. Hardy, D. R. Hart, R. G. Hartley, C. A. Haynam, G. M. Heestand, M. R. Hermann, G. L. Hermes, D. S. Hey, R. L. Hibbard, D. G. Hicks, D. E. Hinkel, D. L. Hipple, J. D. Hitchcock, D. L. Hodtwalker, J. P. Holder, J. D. Hollis, G. M. Holtmeier, S. R. Huber, A. W. Huey, D. N. Hulsey, S. L. Hunter, T. R. Huppler, M. S. Hutton, N. Izumi, J. L. Jackson, M. A. Jackson, K. S. Jancaitis, D. R. Jedlovec, B. Johnson, M. C. Johnson, T. Johnson, M. P. Johnston, O. S. Jones, D. H. Kalantar, J. H. Kamperschroer, R. L. Kauffman, G. A. Keating, L. M. Kegelmeyer, S. L. Kenitzer, J. R. Kimbrough, K. King, R. K. Kirkwood, J. L. Klingmann, K. M. Knittel, T. R. Kohut, K. G. Koka, S. W. Kramer, J. E. Krammen, K. G. Krauter, G. W. Krauter, E. K. Krieger, J. J. Kroll, K. N. La Fortune, and L. J. a. Lagin, Phys. Rev. Lett. **106**, 085004 (2011).
[70]O. S. Jones, C. J. Cerjan, M. M. Marinak, J. L. Milovich, H. F. Robey, P. T. Springer, L. R. Benedetti, D. L. Bleuel, E. J. Bond, D. K. Bradley, D. A. Callahan, J. A. Caggiano, P. M. Celliers, D. S. Clark, S. M. Dixit, T. Doppner, R. J. Dylla-Spears, E. G. Dzentitis, D. R. Farley, S. M. Glenn, S. H. Glenzer, S. W. Haan, B. J. Haid, C. A. Haynam, D. G. Hicks, B. J. Kozioziemski, K. N. LaFortune, O. L. Landen, E. R. Mapoles, A. J. MacKinnon, J. M. McNaney, N. B. Meezan, P. A. Michel, J. D. Moody, M. J. Moran, D. H. Munro, M. V. Patel, T. G. Parham, J. D. Sater, S. M. Sepke, B. K. Spears, R. P. J. Town, S. V. Weber, K. Widmann, C. C. Widmayer, E. A. Williams, L. J. Atherton, M. J. Edwards, J. D. Lindl, B. J. MacGowan, L. J. Suter, R. E. Olson, H. W. Herrmann, J. L. Kline, G. A. Kyrala, D. C. Wilson, J. Frenje, T. R. Boehly, V. Glebov, J. P. Knauer, A. Nikroo, H. Wilkens, and J. D. Kilkenny, Phys. Plasmas **19**, 056315 (2012).
[71]LEH condensate was not a problem on the early *ConA* targets since they used gas-filled capsules, rather than liquid or solid fuel, and thus could be warmed above the condensation temperature. N101218 was warmed to 32 K fifteen minutes prior the shot and cooled again to 24 K at shot time. N101220 was kept at 32 K for the shot. On all subsequent *ConA* experiments, thermally-insulating 'storm' windows (Ref. 17) were used to prevent the formation of the condensate at 24 K.
[72]In this series of shots, an additional 2 × Si graded doped target was shot with a 2 ns slope-of-rise on the main pulse. This was part of an effort to see if the steeper rise would mitigate mix on the DT implosions. The peak power of this shot (N120409) was ~370 TW, higher than the ~330 TW for the 3 ns shot (N120408) reported here. This led to a slightly higher peak velocity but otherwise similar radiographic data. Further information about this shot (N120409) is given in Tables II and III.
[73]B. K. Spears, S. Glenzer, M. J. Edwards, S. Brandon, D. Clark, R. Town, C. Cerjan, R. Dylla-Spears, E. Mapoles, D. Munro, J. Salmonson, S. Sepke, S. Weber, S. Hatchett, S. Haan, P. Springer, E. Moses, J. Kline, G. Kyrala, and D. Wilson, Phys. Plasmas **19**, 056316 (2012).
[74]N. B. Meezan, D. G. Hicks, D. A. Callahan, R. E. Olson, M. S. Schneider, C. A. Thomas, H. F. Robey, P. M. Celliers, J. K. Kline, S. N. Dixit, P. A. Michel, O. S. Jones, D. S. Clark, J. E. Ralph, T. Doeppner, A. J. MacKinnon, S. W. Haan, O. L. Landen, S. H. Glenzer, L. J. Suter, M. J. Edwards, B. J. Macgowan, J. D. Lindl, and L. J. Atherton, in 7th International Conference on Inertial Fusion Sciences and Applications, Bordeaux, France 2011.
[75]The lower-than-expected mass may be caused in part by hydrodynamic instability already present in the ablator. Due to the exponential relation between optical depth and transmission, a given shell mass with high-mode density fluctuations results in less transmission than does a shell of identical mass without these perturbations. However, the fact that similarly low masses were observed (a) Early in the implosion, when mix is expected to be less, and (b) In capsules that have severe mix (see Secs. V B 1 and V C 2)) suggest that mix is not the dominant cause of this low apparent mass.
[76]T. Ma, N. Izumi, R. Tommasini, D. K. Bradley, P. Bell, C. J. Cerjan, S. Dixit, T. Döppner, O. Jones, J. L. Kline, G. Kyrala, O. L. Landen, S. LePape, A. J. Mackinnon, H.-S. Park, P. K. Patel, R. R. Prasad, J. Ralph, S. P. Regan, V. A. Smalyuk, P. T. Springer, L. Suter, R. P. J. Town, S. V. Weber, and S. H. Glenzer, Rev. Sci. Instrum. **83**, 10E115 (2012).
[77]T. H. Cormen, C. E. Leiserson, R. L. Rivest, and C. Stein, *Introduction to Algorithms*, 2nd ed. (MIT, Cambridge, MA, USA, 2001), Chap. 16.